



Phase Field Modeling of Twinning in Indentation of Transparent Crystals

by J. D. Clayton and J. Knap

ARL-RP-340

September 2011

A reprint from Modelling and Simulation in Materials Science and Engineering, Vol. 19, pp. 1–31, 2011.

NOTICES

Disclaimers

The findings in this report are not to be construed as an official Department of the Army position unless so designated by other authorized documents.

Citation of manufacturer's or trade names does not constitute an official endorsement or approval of the use thereof.

Destroy this report when it is no longer needed. Do not return it to the originator.

Army Research Laboratory

Aberdeen Proving Ground, MD 21005-5069

ARL-RP-340**September 2011**

Phase Field Modeling of Twinning in Indentation of Transparent Crystals

J. D. Clayton and J. Knap
Weapons and Materials Research Directorate, ARL

*A reprint from **Modelling and Simulation in Materials Science and Engineering**, Vol. 19, pp. 1–31, 2011.*

REPORT DOCUMENTATION PAGE				Form Approved OMB No. 0704-0188	
Public reporting burden for this collection of information is estimated to average 1 hour per response, including the time for reviewing instructions, searching existing data sources, gathering and maintaining the data needed, and completing and reviewing the collection information. Send comments regarding this burden estimate or any other aspect of this collection of information, including suggestions for reducing the burden, to Department of Defense, Washington Headquarters Services, Directorate for Information Operations and Reports (0704-0188), 1215 Jefferson Davis Highway, Suite 1204, Arlington, VA 22202-4302. Respondents should be aware that notwithstanding any other provision of law, no person shall be subject to any penalty for failing to comply with a collection of information if it does not display a currently valid OMB control number. PLEASE DO NOT RETURN YOUR FORM TO THE ABOVE ADDRESS.					
1. REPORT DATE (DD-MM-YYYY) September 2011		2. REPORT TYPE Reprint		3. DATES COVERED (From - To) August 2010–September 2011	
4. TITLE AND SUBTITLE Phase Field Modeling of Twinning in Indentation of Transparent Crystals				5a. CONTRACT NUMBER	
				5b. GRANT NUMBER	
				5c. PROGRAM ELEMENT NUMBER	
6. AUTHOR(S) J. D. Clayton and J. Knap				5d. PROJECT NUMBER AH80	
				5e. TASK NUMBER	
				5f. WORK UNIT NUMBER	
7. PERFORMING ORGANIZATION NAME(S) AND ADDRESS(ES) U.S. Army Research Laboratory ATTN: RDRL-WMP-B Aberdeen Proving Ground, MD 21005-5069				8. PERFORMING ORGANIZATION REPORT NUMBER ARL-RP-340	
9. SPONSORING/MONITORING AGENCY NAME(S) AND ADDRESS(ES)				10. SPONSOR/MONITOR'S ACRONYM(S)	
				11. SPONSOR/MONITOR'S REPORT NUMBER(S)	
12. DISTRIBUTION/AVAILABILITY STATEMENT Approved for public release; distribution is unlimited.					
13. SUPPLEMENTARY NOTES A reprint from <i>Modelling and Simulation in Materials Science and Engineering</i> , Vol. 19, pp. 1–31, 2011.					
14. ABSTRACT Continuum phase field theory is applied to study elastic twinning in calcite and sapphire single crystals subjected to indentation loading by wedge-shaped indenters. An order parameter is associated with the magnitude of stress-free twinning shear. Geometrically linear and nonlinear theories are implemented and compared, the latter incorporating neo-Hookean elasticity. Equilibrium configurations of deformed and twinned crystals are attained numerically via direct energy minimization. Results are in qualitative agreement with experimental observations: a long thin twin forms asymmetrically under one side of the indenter, the tip of the twin is sharp and the length of the twin increases with increasing load. Qualitatively similar results are obtained using isotropic and anisotropic elastic constants, though the difference between isotropic and anisotropic results is greater in sapphire than in calcite. Similar results are also obtained for nanometer-scale specimens and millimeter-scale specimens. Indentation forces are greater in the nonlinear model than the linear model because of the increasing tangent bulk modulus with increasing pressure in the former. Normalized relationships between twin length and indentation force are similar for linear and nonlinear theories at both nanometer and millimeter scales. Twin morphologies are similar for linear and nonlinear theories for indentation with a 90° wedge. However, in the nonlinear model, indentation with a 120° wedge produces a lamellar twin structure between the indenter and the long sharp primary twin. This complex microstructure is not predicted by the linear theory.					
15. SUBJECT TERMS phase field modeling, twinning, elasticity, meso-scale, ceramics					
16. SECURITY CLASSIFICATION OF:			17. LIMITATION OF ABSTRACT UU	18. NUMBER OF PAGES 38	19a. NAME OF RESPONSIBLE PERSON J. D. Clayton
a. REPORT Unclassified	b. ABSTRACT Unclassified	c. THIS PAGE Unclassified			19b. TELEPHONE NUMBER (Include area code) 410-278-6146

Phase field modeling of twinning in indentation of transparent crystals

J D Clayton¹ and J Knap²

¹ RDRL-WMP-B, US Army Research Laboratory, Aberdeen, MD 21005-5066, USA

² RDRL-CIH-C, US Army Research Laboratory, Aberdeen, MD 21005-5066, USA

E-mail: john.d.clayton1@us.army.mil and jaroslaw.knap@us.army.mil

Received 9 March 2011, in final form 1 August 2011

Published 26 September 2011

Online at stacks.iop.org/MSMSE/19/085005

Abstract

Continuum phase field theory is applied to study elastic twinning in calcite and sapphire single crystals subjected to indentation loading by wedge-shaped indenters. An order parameter is associated with the magnitude of stress-free twinning shear. Geometrically linear and nonlinear theories are implemented and compared, the latter incorporating neo-Hookean elasticity. Equilibrium configurations of deformed and twinned crystals are attained numerically via direct energy minimization. Results are in qualitative agreement with experimental observations: a long thin twin forms asymmetrically under one side of the indenter, the tip of the twin is sharp and the length of the twin increases with increasing load. Qualitatively similar results are obtained using isotropic and anisotropic elastic constants, though the difference between isotropic and anisotropic results is greater in sapphire than in calcite. Similar results are also obtained for nanometer-scale specimens and millimeter-scale specimens. Indentation forces are greater in the nonlinear model than the linear model because of the increasing tangent bulk modulus with increasing pressure in the former. Normalized relationships between twin length and indentation force are similar for linear and nonlinear theories at both nanometer and millimeter scales. Twin morphologies are similar for linear and nonlinear theories for indentation with a 90° wedge. However, in the nonlinear model, indentation with a 120° wedge produces a lamellar twin structure between the indenter and the long sharp primary twin. This complex microstructure is not predicted by the linear theory.

(Some figures in this article are in colour only in the electronic version)

1. Introduction

Twinning is a fundamental deformation mechanism that occurs in many crystalline solids. In this work, phase field theory is used to model deformation twinning, also known as mechanical

twinning, which is defined as twinning induced by mechanical stresses [1–3]. Deformation twinning is henceforth simply referred to as ‘twinning’. The transformation strain associated with twinning is a simple shear. Across the habit plane, the orientation of the Bravais lattice differs by a reflection or rotation depending on the kind of twin under consideration. The sheared and reoriented crystal is labeled the ‘twin’, while the region of crystal that maintains its original lattice orientation is labeled the ‘parent’ or the ‘matrix’. At the atomic scale, twinning takes place by coordinated movement of partial dislocations (i.e. twinning dislocations) and/or atomic shuffles [2]. A finite surface energy can be associated with the twin boundary, often estimated on the order of the appropriate stacking fault energy [4]. The interfacial energy of a growing or shrinking twin can also include elastic and core energies of twinning dislocations comprising such interfaces, often labeled ‘incoherent interfaces’ [1]. Although exceptions exist, deformation twinning is often a preferred deformation mechanism in crystals with low stacking fault energy and/or low crystallographic symmetry [2].

Twinning in calcite (CaCO_3) was extensively characterized via a number of experiments in the mid-20th century [1, 5–11]. At room temperature, dislocation glide does not occur readily in calcite, but twinning can occur profusely [10]. Thus, calcite is an ideal material for validation of models of deformation twinning, since twin morphologies can be observed using optical measurements (a benefit of calcite’s transparency), and since dislocation-mediated plasticity need not be addressed.

A number of experimental studies of twinning in calcite considered indentation loading, either with knife-edge indenters [5, 7, 9] or with spherical indenters [8]. Calcite crystals were oriented such that the direction of twinning shear was parallel to the loading direction and the habit plane normal was perpendicular to the loading direction. Twinning under such conditions was often reported to be ‘elastic’, that is, twins under the indenter disappeared fully or partially upon load removal [1, 5, 8, 11]. Twins originated at the contact surface and were reported to be thin with a sharp tip or apex as shown in figure 1, with the length of the twin increasing with increasing load. Twins could be maintained in a stable position (i.e. held at a constant length) when the load was held fixed, with measured sizes reported on the order of micrometers to hundreds of μm depending on the magnitude of applied load and type of indenter geometry [1, 5, 8, 11]. When the calcite crystals exhibit no surface defects, twins appear only after a threshold load is applied, whereas twins can appear immediately (i.e. upon application of a minimal load) at surface imperfections when the crystals exhibit such defects [8]. The title of this work is motivated by the transparency of calcite (and sapphire, as discussed later) which enables direct optical observation of elastic twinning during indentation loading. Appearance and disappearance of elastic twins cannot be visually observed within opaque materials such as metals.

Previous analytical models have offered a partial description of physics of elastic twinning under concentrated loading but cannot be categorized as fully predictive in terms of twin morphology or elastic fields. Lifshitz [12]—see summary of model in English language in [1]—incorporated a nonlinear elastic law (with non-convex energy density) and showed that a two-dimensional twin of finite thickness should terminate within the material at a corner point with zero aperture angle, i.e. a sharp cusp. This theory [1, 12] does not incorporate dislocation mechanics or any quantitative value of interfacial energy and does not enable prediction of the size of the twin, but it does give qualitative information regarding the twin’s equilibrium shape.

A different theory developed by Kosevich and colleagues [1, 9, 11] assumes *a priori* that the twin is long and thin and can be modeled as a one-dimensional continuum elasticity problem. This theory considers, for equilibrium, a balance of forces of linear elastic origin, Peierls forces [13] associated with lattice friction, and surface tension forces that resist the

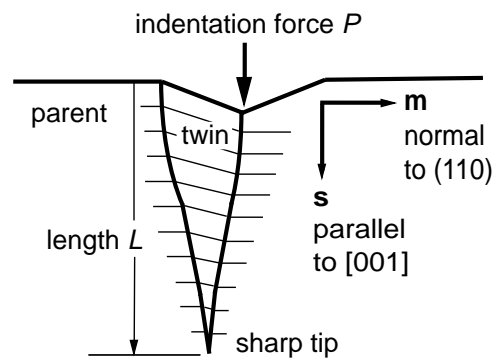


Figure 1. Wedge-shaped twin in calcite, after Kosevich and Boiko [1]. Twin appears only under left side of indenter because shear deformation under right side is directed in anti-twinning sense.

formation of stacking faults in the region of extension of the twin (i.e. at the tip). Linear elastic forces are assumed to arise from a continuous distribution of twinning (partial) dislocations comprising the interface. The thickness of a one-dimensional twin at a point is related to the dislocation density distribution. Phenomenological parameters in this theory can be prescribed so that the analytical solution matches experimental measurements of twin length and applied indentation force [1, 9, 11], but the theory cannot be regarded as fully predictive because such parameters are not obtained from independent measurements.

Crystal plasticity-type models have also been developed to describe twinning. In such models, the volume or mass fraction of a given material element occupied by twins belonging to one or more twin systems is treated as an internal state variable that evolves with thermomechanical loading via a kinetic law. Transformation kinetics are typically controlled by driving stress and/or temperature. These models are useful for describing texture evolution [14, 15] and macroscopic stress–strain behavior [3, 16–18]. A crystal mechanics approach has also been used to predict subgrain twin morphology in 3D polycrystal simulations [19].

In this paper, a phase field theory for twinning developed recently by the authors [20] is used. In any given simulation, twinning is restricted to occur on only one twin system. An order parameter gauges the magnitude twinning shear on this system at any location in the problem domain. The general form of the model in [20] accounts for large deformations, nonlinear and anisotropic mechanical elastic properties, and anisotropic surface energy associated with twin boundaries. Equilibrium configurations of deformed and twinned crystals are attained via direct energy minimization. The theory is framed in the null temperature (i.e. 0 K) limit, with no account of dissipation or irreversibility. Model assumptions of static equilibrium and null dissipation are deemed particularly appropriate for a study of ‘elastic’ twinning in indented calcite. Apart from the geometry of the twin system (shearing plane, direction and magnitude) known *a priori* from the crystal structure, the only material properties entering the present phase field model are the elastic constants which are known from experiments [21], and the twin boundary energy and characteristic thickness, which are known from atomic calculations [22]. Hence, the model is deemed fully predictive because morphologies and elastic fields associated with twinning do not result from any *a priori* assumptions on twin shape or kinetics of inelastic material behavior.

In phase field modeling, interfaces between pure phases—in the present case between twinned and untwinned regions of crystal—possess a finite thickness. Boundary value problems incorporating diffuse interface theory are amenable to treatment with modern numerical methods [23, 24]. In contrast, sharp interface models that address equilibrium or

stability among phases of nonlinear elastic materials (including deformation twins) have been examined extensively using analytical methods [25–29], and less so with numerical techniques.

In addition to calcite, sapphire is also considered. Sapphire is the single crystal form of α -alumina (Al_2O_3), and is alternatively referred to in various literature as corundum. High-purity sapphire, like calcite, is transparent. Results for sapphire provide a useful basis for comparison with those for calcite. Sapphire is notably stiffer (much higher hardness and elastic constants) than calcite. Calcite and sapphire belong to the same crystallographic space group; both are trigonal. Twinning in sapphire can occur on either of two twin systems (on basal or rhombohedral planes) [16, 18, 30, 31]; both twin systems are considered individually in this work. Dislocation plasticity (i.e. plastic slip) can accompany twinning in sapphire subjected to indentation loading [32–34], since critical resolved shear stresses required to induce twinning and slip are of the same order of magnitude [16, 18]. Because the model and results presented here do not consider plastic slip, they represent idealized behavior. The present model would require substantial changes to address kinematics and kinetics of dislocation distributions and plastic slip [3, 16–18, 35], with corresponding dissipation.

Reported first in this paper are predictions for linear elastic behavior. In the present phase field model [20], when elastic strains are small, the difference in driving shear stress for twinning is a factor on the order of twinning shear. Previous theoretical studies of homogeneous twin nucleation [2, 36, 37] have relied on linear elasticity, presumably because analytical solutions are not feasible for nonlinear models. The geometrically linear model considered in this work enables direct comparison with analytical solutions of wedge indentation in elastic and elastic–plastic materials [38–40]. Geometrically linear theory has also been applied elsewhere towards phase field modeling of twinning [41].

Reported second in this paper are model predictions for a finite strain model incorporating nonlinear elastic behavior. Results from nonlinear and linear theories are also compared directly. Linear theory can provide qualitative insight and in some cases quantitatively reasonable descriptions of phase transformations and twinning behavior [29]. However, in other cases, linear and nonlinear models can yield drastically different results with regards to both analytical/theoretical predictions [29] and numerical predictions of phase field models [42]. Results reported in this paper demonstrate qualitative agreement between linear and nonlinear models for some phenomena, but significant differences for others. The theory and results presented here incorporate a neo-Hookean model [43, 44] for nonlinear elastic behavior, thus presuming an isotropic elastic response. Such an assumption is thought justified since differences in predictions among isotropic and anisotropic linear elastic models are not drastic, with qualitatively similar twin sizes and shapes obtained for isotropic and anisotropic elasticity.

The rest of this paper is organized as follows. The phase field theory is summarized in section 2, applicable to any generic crystalline material undergoing the same deformation mechanisms. Properties of calcite and sapphire are addressed in section 3. Numerical application of the linear theory to indentation is discussed in section 4; application of the nonlinear theory in section 5. Conclusions follow in section 6.

Notation of continuum mechanics is used. Familiarity of the reader with elasticity theory and phase field modeling is assumed; overviews of the latter include [23, 24]. Vectors and higher-order tensors are written in bold italic font; scalars and components of vectors and tensors are written in italic font. When indicial notation is used, summation proceeds over repeated indices. Vectors and tensors are referred to a fixed Cartesian frame of reference, with indices in the subscript position. The scalar product of vectors \mathbf{a} and \mathbf{b} is $\mathbf{a} \cdot \mathbf{b} = a_A b_A = a_1 b_1 + a_2 b_2 + a_3 b_3$ in three-dimensional space. The outer product is $(\mathbf{a} \otimes \mathbf{b})_{AB} = a_A b_B$. Juxtaposition implies summation over one set of adjacent indices,

e.g., $(AB)_{AB} = A_{AC}B_{CB}$. The colon denotes summation over two sets of indices, e.g., $A : B = A_{AB}B_{AB}$. A T superscript denotes the transpose, e.g., $A_{AB}^T = A_{BA}$.

2. Theory

A continuum phase field theory for twinning [20] is summarized. The theory for geometrically linear kinematics is presented first, followed by the finite strain theory.

2.1. Linear theory

Let $X \in \Omega$ be a material point. The order parameter function is $\eta(X, t)$, where t denotes time. The order parameter distinguishes between two phases: (i) the original crystal (the parent) and (ii) the twin. Interfaces between phases are twin boundaries. Order parameter η generally exhibits the following values:

$$\begin{aligned} \eta(X, \bullet) &= 0 \forall X \in \text{parent}, \\ &= 1 \forall X \in \text{twin}, \\ &\in (0, 1) \forall X \in \text{twin boundaries}. \end{aligned} \quad (1)$$

In linear elasticity, kinematic field variables are displacement \mathbf{u} and its gradient

$$\boldsymbol{\beta} = \nabla \mathbf{u}, \quad \beta_{AB} = \nabla_B u_A. \quad (2)$$

The distortion is split additively as

$$\boldsymbol{\beta} = \boldsymbol{\beta}^E + \boldsymbol{\beta}^\eta, \quad (3)$$

where $\boldsymbol{\beta}^E$ is the elastic distortion and $\boldsymbol{\beta}^\eta$ is the stress-free distortion associated with the twinning shear or twinning transformation:

$$\boldsymbol{\beta}^\eta = [\varphi(\eta)] \gamma_0 \mathbf{s} \otimes \mathbf{m}. \quad (4)$$

The unit normal to the surface of composition (i.e. the habit plane) is \mathbf{m} . The magnitude of the twinning shear and the shear direction are γ_0 and \mathbf{s} , respectively. The following conditions hold: $\mathbf{m} \cdot \mathbf{m} = \mathbf{s} \cdot \mathbf{s} = 1$ and $\mathbf{s} \cdot \mathbf{m} = 0$.

Interpolation function φ relates twinning distortion and the order parameter [42]:

$$\varphi(\eta) = 3\eta^2 - 2\eta^3. \quad (5)$$

Note that φ is a monotonically increasing function obeying $\varphi(0) = 0$, $\varphi(1) = 1$, with vanishing derivatives with respect to η at its endpoints: $\varphi'(0) = \varphi'(1) = 0$. This function also obeys the anti-symmetry conditions $\varphi(1 - \eta) = 1 - \varphi(\eta)$. The symmetric elastic strain tensor is

$$\begin{aligned} \boldsymbol{\epsilon}^E(\nabla \mathbf{u}, \eta) &= \frac{1}{2} \left\{ \boldsymbol{\beta}^E + \boldsymbol{\beta}^{E^T} \right\} \\ &= \frac{1}{2} \left\{ \nabla \mathbf{u} + (\nabla \mathbf{u})^T - \gamma_0 [\varphi(\eta)] [\mathbf{s} \otimes \mathbf{m} + \mathbf{m} \otimes \mathbf{s}] \right\}. \end{aligned} \quad (6)$$

The total free energy functional for a body of volume Ω is written as

$$\Psi(\mathbf{u}, \eta) = \int_{\Omega} W(\nabla \mathbf{u}, \eta) d\Omega + \int_{\Omega} f(\eta, \nabla \eta) d\Omega, \quad (7)$$

where W is the elastic strain energy density and f accounts for interfacial energy. Strain energy density and second-order elastic moduli are

$$W = W[\boldsymbol{\epsilon}^E(\nabla \mathbf{u}, \eta), \eta] = \frac{1}{2} \epsilon_{AB}^E C_{ABCD}(\eta) \epsilon_{CD}^E, \quad (8)$$

$$C_{ABCD}(\eta) = \left. \frac{\partial^2 W}{\partial \epsilon_{AB}^E \partial \epsilon_{CD}^E} \right|_{\epsilon^E = \mathbf{0}}. \quad (9)$$

For a centrosymmetric structure, a re-orientation matrix \mathbf{Q} associated with twinning is the reflection [2, 3]

$$\mathbf{Q} = \mathbf{1} - 2\mathbf{m} \otimes \mathbf{m}, \quad (10)$$

with $\mathbf{1}$ the unit tensor. Elastic coefficients of the fully twinned crystal are related to those of the parent by

$$C_{ABCD}(1) = Q_{AE}Q_{BF}Q_{CG}Q_{DH}C_{EFGH}(0). \quad (11)$$

Elastic coefficients in interfacial regions are interpolated as

$$C_{ABCD}(\eta) = C_{ABCD}(0) + [C_{ABCD}(1) - C_{ABCD}(0)]\varphi(\eta). \quad (12)$$

When isotropic elasticity is used, elastic coefficients are independent of orientation:

$$C_{ABCD} = \lambda\delta_{AB}\delta_{CD} + \mu(\delta_{AC}\delta_{BD} + \delta_{AD}\delta_{BC}), \quad (13)$$

with λ and μ the Lamé constant and shear modulus; hence in the isotropic case W does not explicitly depend on η .

The local interfacial energy per unit volume is

$$f(\eta, \nabla\eta) = f_0(\eta) + \kappa(\eta) : (\nabla\eta \otimes \nabla\eta), \quad (14)$$

with κ a symmetric second-order tensor. For anisotropic surface energy, $\kappa_{AB}(\eta) = \kappa_{AB}(0) + \zeta\varphi(\eta)[\kappa_{AB}(1) - \kappa_{AB}(0)]$, where similarly to (12), $\kappa_{AB}(1) = Q_{AC}Q_{BD}\kappa_{CD}(0)$, and where $\zeta \in [0, 1]$ is a scalar constant. Case $\zeta = 0$ considered in previous work [20] implies that the gradient contribution to interfacial energy is invariant with respect to η and hence the twinning shear; condition $\zeta = 1$ implies that the gradient contribution depends on the transformation of the lattice (e.g. reflection) associated with twinning. Other models have included highly anisotropic surface energy [41]. When interfacial energy is isotropic, $\kappa = \kappa\mathbf{1}$ and

$$f(\eta, \nabla\eta) = f_0(\eta) + \kappa|\nabla\eta|^2. \quad (15)$$

Prescribed for f_0 is a standard ‘double-well’ potential:

$$f_0(\eta) = A\eta^2(1 - \eta)^2, \quad (16)$$

with $A > 0$. In the isotropic approximation A and κ are related to equilibrium energy per unit area Γ and thickness l of an unstressed interface via [20]

$$\kappa = 3\Gamma l/4, \quad A = 12\Gamma/l. \quad (17)$$

In this work, both f_0 and $\nabla\eta$ contribute to what is called interfacial energy (14). This label follows the scheme denoted in (1): by the convention used here, values of $\eta \neq 0, 1$ designate ‘interface’, so $f = 0$ wherever $\eta = 0, 1$. Other presentations may use different notation, e.g. f_0 has been labeled ‘deformation energy’ in another phase field model for twinning [41], since a uniform value of the order parameter differing from zero or unity can result in a finite energetic contribution. It is also noted that (15) with (16) constitute a simple assumption regarding interfacial energy; more elaborate models accounting for additional physics (e.g. more than two variants, anisotropic dislocation core and stacking fault contributions, or grain boundary misorientation and cusps associated with low-energy boundaries) exist [41, 45–48].

The following variational equation is posited that will yield equilibrium equations and boundary conditions:

$$\delta\Psi = \oint_{\partial\Omega} \mathbf{t} \cdot \delta\mathbf{u} \, dS + \oint_{\partial\Omega} h \, \delta\eta \, dS, \quad (18)$$

where \mathbf{t} is a mechanical traction vector per unit area, dS is a surface element of $\partial\Omega$ and h is a scalar conjugate force to variations of the order parameter. Euler–Lagrange equations obtained from (18) are [20]

$$\nabla \cdot \frac{\partial W}{\partial \nabla \mathbf{u}} \Big|_{\eta} = \nabla \cdot \boldsymbol{\sigma} = 0, \quad f'_0 - 2\nabla \cdot (\boldsymbol{\kappa} \nabla \eta) + \frac{\partial W}{\partial \eta} \Big|_{\nabla \mathbf{u}} = 0, \quad (19)$$

where $\boldsymbol{\sigma}$ is the symmetric stress tensor. Corresponding boundary conditions are

$$\mathbf{t} = \boldsymbol{\sigma} \mathbf{n}, \quad h = 2\boldsymbol{\kappa} : (\nabla \eta \otimes \mathbf{n}), \quad (20)$$

where \mathbf{n} is the unit outward normal to $\partial\Omega$. The stress also obeys the usual linear elasticity relationship

$$\sigma_{AB} = C_{ABCD} \epsilon_{CD}^E. \quad (21)$$

The second of equilibrium conditions (19) can be rewritten as

$$\begin{aligned} f'_0 = & 2\nabla_A (\kappa_{AB} \nabla_B \eta) + \varphi' \{ \tau \gamma_0 + \zeta \nabla_A \eta \nabla_B \eta [\kappa_{AB}(0) - \kappa_{AB}(1)] \\ & + (1/2) \epsilon_{AB}^E \epsilon_{CD}^E [C_{ABCD}(0) - C_{ABCD}(1)] \}, \end{aligned} \quad (22)$$

where the driving shear stress for twinning is

$$\tau = \boldsymbol{\sigma} : (\mathbf{s} \otimes \mathbf{m}). \quad (23)$$

For isotropic surface and elastic energies, with φ from (5) and f_0 from (16), equilibrium condition (22) becomes

$$3\tau \gamma_0 \eta (1 - \eta) = A\eta (1 - 3\eta + 2\eta^2) - \kappa \nabla^2 \eta. \quad (24)$$

Both sides of (22) and (24) vanish in regions of uniform phase where $\eta = 0$ or $\eta = 1$.

2.2. Nonlinear theory

Equations (1), (5) and (14)–(17) also apply for the nonlinear theory. Spatial \mathbf{x} and referential \mathbf{X} coordinates of a material particle are related by the motion

$$\mathbf{x} = \boldsymbol{\chi}(\mathbf{X}, t). \quad (25)$$

The deformation gradient is

$$\mathbf{F} = \nabla \boldsymbol{\chi}, \quad F_{aA} = \nabla_A \chi_a, \quad (26)$$

with $\nabla_A = \partial/\partial X_A$. The deformation gradient is decomposed multiplicatively as

$$\mathbf{F} = \mathbf{F}^E \mathbf{F}^\eta, \quad (27)$$

where $\mathbf{F}^E = \mathbf{F} \mathbf{F}^{\eta-1}$ is the elastic deformation and $\mathbf{F}^\eta[\eta(\mathbf{X}, t)]$ represents the stress-free twinning shear. For twinning on a single system, the following form applies:

$$\mathbf{F}^\eta = \mathbf{1} + [\varphi(\eta)] \gamma_0 \mathbf{s} \otimes \mathbf{m}. \quad (28)$$

The unit (identity) tensor is $\mathbf{1}$. The symmetric elastic deformation tensor is

$$\mathbf{C}^E = \mathbf{F}^{E\top} \mathbf{F}^E, \quad C_{\alpha\beta}^E = F_{a\alpha}^E F_{a\beta}^E. \quad (29)$$

Twinning is isochoric:

$$J^\eta = \det \mathbf{F}^\eta = 1 + [\varphi(\eta)] \gamma_0 \mathbf{s} \cdot \mathbf{m} = 1. \quad (30)$$

It follows that

$$J = \det \mathbf{F} = \det \mathbf{F}^E \det \mathbf{F}^\eta = J^E J^\eta = J^E = \sqrt{\det \mathbf{C}^E}. \quad (31)$$

The total energy functional for a body of initial (i.e. undeformed) volume Ω is

$$\Psi(\chi, \eta) = \int_{\Omega} W(\mathbf{F}, \eta) \, d\Omega + \int_{\Omega} f(\eta, \nabla \eta) \, d\Omega, \quad (32)$$

where W is the elastic strain energy density and f accounts for interfacial energy. For a neo-Hookean material [44], strain energy density

$$W = W[\mathbf{C}^E(\mathbf{F}, \eta)] = \frac{\lambda}{2}(\text{tr} \mathbf{C}^E - 3) + \ln J \left(\frac{\lambda}{2} \ln J - \mu \right). \quad (33)$$

For a (deviatoric) simple shear deformation gradient, the response of a neo-Hookean material is the same as that for a linear elastic material with the same shear modulus. On the other hand, when large volume changes are involved, predictions of neo-Hookean and linear elastic models can differ significantly. Specifically, as will be demonstrated later in section 3, a neo-Hookean model can describe the usual increase in tangent bulk modulus with increasing compressive pressure.

The following variational equation is posited that will yield equilibrium equations and boundary conditions:

$$\delta \Psi = \oint_{\partial \Omega} \mathbf{t} \cdot \delta \chi \, dS + \oint_{\partial \Omega} h \, \delta \eta \, dS, \quad (34)$$

where \mathbf{t} is a mechanical traction vector per unit reference area, dS is a surface element of $\partial \Omega$, and h is a scalar conjugate force to variations of the order parameter. Application of the divergence theorem, integration by parts, and localization of (34) lead to the Euler–Lagrange equations [20]:

$$\nabla \cdot \frac{\partial W}{\partial \mathbf{F}} \Big|_{\eta} = \nabla \cdot \mathbf{P} = 0, \quad f'_0 - 2\kappa \nabla^2 \eta + \frac{\partial W}{\partial \eta} \Big|_{\mathbf{F}} = 0, \quad (35)$$

with \mathbf{P} the first Piola–Kirchhoff stress. Corresponding boundary conditions are

$$\mathbf{t} = \mathbf{P} \mathbf{n}, \quad h = 2\kappa \nabla \eta \cdot \mathbf{n}, \quad (36)$$

where \mathbf{n} is the unit outward normal to $\partial \Omega$.

The first Piola–Kirchhoff stress satisfies

$$\mathbf{P} = \frac{\partial W}{\partial \mathbf{F}} \Big|_{\eta} = \frac{\partial W}{\partial \mathbf{C}^E} : \frac{\partial \mathbf{C}^E}{\partial \mathbf{F}^E} : \frac{\partial \mathbf{F}^E}{\partial \mathbf{F}} \Big|_{\eta} = \mathbf{F}^E \Sigma \mathbf{F}^{\eta^{-T}}. \quad (37)$$

The following kinematic identities prove useful for neo-Hookean elasticity:

$$\frac{\partial \ln J}{\partial \mathbf{C}^E} = \frac{1}{2} \mathbf{C}^{E-1}, \quad \frac{\partial \mathbf{C}^{E-1}_{\alpha\chi}}{\partial \mathbf{F}^E_{b\beta}} = -\mathbf{F}^{E-1}_{\alpha b} \mathbf{C}^{E-1}_{\beta\chi} - \mathbf{F}^{E-1}_{\chi b} \mathbf{C}^{E-1}_{\alpha\beta}. \quad (38)$$

The symmetric elastic second Piola–Kirchhoff stress is obtained from (33) and (37) as

$$\Sigma = 2 \frac{\partial W}{\partial \mathbf{C}^E} = \mu \mathbf{1} + (\lambda \ln J - \mu) \mathbf{C}^{E-1}. \quad (39)$$

The second of equilibrium conditions (19) can be rewritten as

$$f'_0 = 2\kappa \nabla^2 \eta + \tau \gamma_0 \varphi', \quad (40)$$

where the driving shear stress for twinning is

$$\begin{aligned} \tau &= -\frac{1}{\gamma_0 \varphi'} \frac{\partial W}{\partial \eta} \Big|_{\mathbf{F}} = -\frac{1}{\gamma_0 \varphi'} \frac{\partial W}{\partial \mathbf{C}^E} : \frac{\partial \mathbf{C}^E(\mathbf{F}, \eta)}{\partial \eta} \Big|_{\mathbf{F}} \\ &= \Sigma : [\mathbf{C}^E(\mathbf{s} \otimes \mathbf{m}) \mathbf{F}^{\eta^{-1}}]. \end{aligned} \quad (41)$$

Using (5), (16) and (41), equilibrium condition (40) can then be written as in (24).

It can be shown [20], given certain boundary conditions, that a (meta)stable configuration of a body undergoing twinning corresponds to a (local) minimizer of energy functional Ψ of (32). Thus the mathematical problem of interest whose solution is sought numerically, as described later in sections 4 and 5, can be stated simply as

$$\min_{\chi, \eta} \Psi(\chi, \eta). \quad (42)$$

3. Materials

Relevant behaviors of calcite and sapphire are discussed; requisite material properties associated with elasticity and twinning in each material are tabulated.

3.1. Calcite

Calcite is a stable low-temperature polymorph of calcium carbonate (CaCO_3), and is an ionic crystal with trigonal (i.e. rhombohedral) symmetry [49, 50]. Transparent single crystals are also called iceland spar. Information regarding the primitive unit cell and requisite properties of calcite are listed in table 1 with supporting references. Calcite belongs to space group $R\bar{3}c$ and centrosymmetric point group $\bar{3}m$. The primitive rhombohedral unit cell is described by lattice parameter a and bond angle α . The primitive cell contains ten atoms (two CaCO_3 formula units); several additional parameters are needed to fully describe the polyatomic structure and can be found elsewhere [50]. Hexagonal crystallographic notation is sometimes used to describe calcite [14, 36, 50], which exhibits four different kinds of twin systems [22]. For the e^+ system considered here, the shear is large: $\gamma_0 = 0.694$. Miller indices shown in figure 1 for shearing direction and habit plane, $\langle 001 \rangle \{110\}$, correspond to the cleavage rhombohedral pseudocell [51] rather than the primitive unit cell of the Bravais lattice.

Twin boundary surface energy is obtained from lattice statics (0 K) calculations conducted elsewhere [22] using an empirical potential [52]. In most phase field simulations discussed later, surface energy is assumed isotropic, following usual theoretical studies [36, 37], but in one case anisotropy of the surface energy is considered. In a material coordinate system with axes aligned parallel to twinning direction and habit plane normal ($X_1 || m$ and $X_2 || s$), the gradient coefficient entering (14) is written [20, 41] as

$$[\kappa] = \begin{bmatrix} \kappa_{11} & 0 \\ 0 & \kappa_{22} \end{bmatrix}. \quad (43)$$

In the isotropic case, $\kappa_{11} = \kappa_{22} = \kappa$. The anisotropic case considered later is $\kappa_{22} = 4\kappa_{11} = 4\kappa$, which would seem to favor boundaries extended parallel to the habit plane. Recall from (17) that surface energy $\Gamma \propto \kappa^{1/2}$. The rationale for anisotropic surface energy is that twinning dislocations at a moving portion of the boundary (i.e. an incoherent interface [1, 20, 41]) would contribute core and elastic energies to the total surface energy of the interface. In contrast, the fully formed (i.e. coherent) twin boundary surface would have less energy than such a moving portion because it does not contain energy of dislocations, just stacking fault energy associated with reflection of the lattice across the twin boundary. Anisotropic values considered here are anticipated to cause the twin to elongate in the direction of s and shorten in the direction of m , in order to decrease the contribution of $\kappa_{22}(\nabla_2 \eta)^2$ to the energy in (14). It is also assumed that κ does not depend on η and hence $\zeta = 0$ in (22).

Equilibrium thickness l over which atoms deviate from their ideal positions is chosen as 1 nm, corresponding to about five $\{110\}$ planes. This value follows from atomic simulations of twin boundaries in calcite [22], where it is reported that the relaxed crystal structure differs

Table 1. Properties of calcite single crystals.

Parameter	Value	Definition	Reference
a	6.201	lattice parameter (Å)	[50]
α	48.3°	rhombohedral angle	[50]
γ_0	0.694	shear for e^+ twin	[14, 36]
C_{11}	165.4 (148.1)	elastic constants 0 K (300 K) (GPa)	[21]
C_{12}	65.0(55.8)		
C_{13}	61.6(54.6)	Lamé modulus 0 K (300 K) (GPa)	[54]
C_{14}	−22.8(−20.6)		
C_{33}	89.5(85.6)	shear modulus 0 K (300 K) (GPa)	[22]
C_{44}	36.6(32.7)		
λ	61.7(54.6)	bulk modulus 0 K (300 K) (GPa)	[54]
μ	40.2(36.7)		
K	88.5(79.1)	$(\partial K / \partial p)_{p=0}$	[54]
K'	4.0		
Γ	183	twin boundary energy (mJ m^{-2})	[22]
l	1.0	twin boundary thickness (nm)	[22, 42]

from that of the bulk mainly over five atomic layers. The same characteristic thickness value (1 nm) has also been used in phase field models of other crystalline materials [20, 42].

Voigt's notation [3, 53] is used for elastic constants in table 1. In simulations discussed later, both isotropic and anisotropic elasticity models are considered. In the former, Voigt-averaged elastic constants [3, 4, 53] are used:

$$\lambda = \frac{1}{15}(C_{11} + 5C_{12} + 8C_{13} + C_{33} - 4C_{44}), \quad (44)$$

$$\mu = \frac{1}{30}(7C_{11} - 5C_{12} - 4C_{13} + 2C_{33} + 12C_{44}). \quad (45)$$

Elastic anisotropy of calcite is significant: $C_{33} \approx 0.5C_{11}$, $C_{14} \approx -0.6C_{44}$ and $C_{44} \approx 0.7C_{66}$. Recall also that for the trigonal crystal class of calcite, $C_{22} = C_{11}$, $C_{24} = -C_{14}$ and $2C_{66} = C_{11} - C_{12}$. In simulations that follow, elastic constants measured at 160 K [21] are extrapolated to 0 K for use in idealized simulations of twinning at the nanoscale (indenter size on the order of nm), in strict adherence to the theoretical model of section 2 and [20] that does not consider dissipation or thermal phenomena. Zero temperature solutions are also more amenable to comparison with predictions of lattice statics [22]. On the other hand, room temperature elastic constants are used in later simulations of indentation at the laboratory scale (indenter size on the order of mm).

To validate the use of a neo-Hookean model for calcite, the response of the material under purely volumetric deformation, $\mathbf{F} = J^{1/3}\mathbf{1}$, is computed and compared with the linear elastic response and that for the Birch equation of state (EOS) [55], where the latter incorporates the bulk modulus K and the pressure derivative of the bulk modulus K' measured experimentally [54]. Specifically, Cauchy pressure p is computed for each elastic constitutive model via

$$p = K(1 - J) \quad (\text{linear elasticity}), \quad (46)$$

$$p = \mu(J^{-1} - J^{-1/3}) - \lambda J^{-1} \ln J \quad (\text{neo-Hookean}), \quad (47)$$

$$p = \frac{3K}{2}J^{-7/3}(1 - J^{-2/3}) \left[1 + \frac{3}{4}(K' - 4)(J^{-2/3} - 1) \right] \quad (\text{Birch EOS}). \quad (48)$$

Results of the calculations for calcite are compared in figure 2(a). In each case, the pressure is normalized by the same value of Voigt-averaged bulk modulus from table 1, $K_V = 79.1$ GPa.

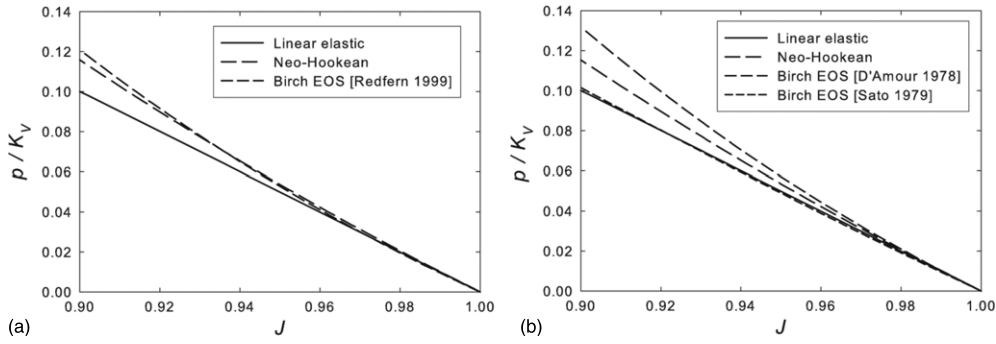


Figure 2. Cauchy pressure (normalized by Voigt-averaged bulk modulus) versus volume for linear and nonlinear elasticity models of (a) calcite and (b) sapphire.

Close agreement is observed between predictions from the neo-Hookean model to be used in simulations and those from the Birch EOS that is fit to experimental data [54]. Note that the response for each of the two nonlinear models is stiffer than that of linear elasticity at higher pressures.

A polymorphic phase transition from trigonal to a monoclinic structure has been observed in calcite deformed under hydrostatic compression at pressures on the order of 1.5 GPa [54, 56]. Evidence of such a phase transformation has not been reported for indentation experiments on calcite [1, 5, 7–11]. However, it is plausible that such a transformation could occur, given the high pressures that exist immediately beneath the indenter that can easily exceed the transformation pressure. For a wedge indenter with a sharp tip, the analytical elastic solution (linear elasticity, in the absence of twinning) suggests that the pressure immediately beneath the tip of the wedge tends to infinity [38, 40]. The phase field theory and simulations described in this work do not address the possibility of this phase transformation in calcite.

3.2. Sapphire

Sapphire is a stable low-temperature polymorph of alumina (Al_2O_3), and like calcite exhibits trigonal symmetry [18, 30]. Sapphire is alternatively known as $\alpha\text{-Al}_2\text{O}_3$ or corundum; nominally colorless when pure, sapphire with trace amounts of secondary elements often exhibits blue or red tints, with red corundum commonly called ruby. Information regarding the primitive unit cell and requisite properties of sapphire are listed in table 2. Like calcite, sapphire belongs to space group $R\bar{3}c$ and centrosymmetric point group $\bar{3}m$. The primitive cell contains ten atoms (two Al_2O_3 formula units); several additional parameters are needed to fully describe the polyatomic structure [30]. Hexagonal crystallographic notation is typically used to describe sapphire [16, 18, 30], which exhibits two kinds of twin systems [16, 18, 30, 31]. The basal (B) system corresponds to $\langle 1\bar{1}00 \rangle \{0001\}$ in the structural unit cell [30], and the shear is large: $\gamma_0 = 0.635$. The rhombohedral (R) system corresponds to $\langle 1\bar{1}0\bar{1} \rangle \{1\bar{1}02\}$ in the structural cell, and the shear is somewhat smaller: $\gamma_0 = 0.202$.

Again, both isotropic and anisotropic elasticity models are considered. In the former, Voigt-averaged elastic constants [53] are used. Elastic anisotropy of sapphire is mild: $C_{33} \approx C_{11}$, $C_{14} \approx 0.16C_{44}$ and $C_{44} \approx 0.9C_{66}$. In the simulations that follow, temperature dependence of elastic coefficients where available [57] is used to provide 0 K constants for use at the nanoscale; room temperature constants [58] are used in simulations of indentation at the laboratory (mm) scale. Following [3, 4, 16, 18], surface energies of twin boundaries are

Table 2. Properties of sapphire single crystals.

Parameter	Value	Definition	Reference
a	5.12	lattice parameter (\AA)	[30]
α	55.3°	rhombohedral angle	[30]
γ_0	0.635	shear for basal (B) twin	[30]
	0.202	shear for rhombohedral (R) twin	[31]
C_{11}	500.0 (498.0)	elastic constants 0 K (300 K) (GPa)	[57, 58]
C_{12}	167.8 (163.0)		
C_{13}	120.5 (117.0)		
C_{14}	23.7 (23.0)		
C_{33}	502.0 (502.0)	Lamé modulus 0 K (300 K) (GPa)	[61]
C_{44}	151.0 (147.0)		
λ	146.7 (144.2)		
μ	166.5 (165.7)		
K	257.7 (254.7)	bulk modulus 0 K (300 K) (GPa)	[62]
	(254.4)		
	(239.0)		
K'	4.3	$(\partial K / \partial p)_{p=0}$	[61]
	0.9		
Γ	745	B twin boundary energy (mJ m^{-2})	[60]
	125	R twin boundary energy (mJ m^{-2})	[59]
l	1.0	twin boundary thickness (nm)	[63, 42]

estimated as half of corresponding stacking fault energies, the latter determined experimentally [59] or through atomic modeling [60].

Use of a neo-Hookean model for sapphire is validated for volumetric compression deformation in figure 2(b), where pressures are computed as in section 3.1. Pressures obtained from the neo-Hookean model are intermediate to those from the Birch EOS fitted to two different sets of hydrostatic compression experiments [61, 62]. The Birch EOS with K and K' from [62] gives predictions very similar to a linear elastic model incorporating Voigt-averaged bulk modulus $K_V = 254.7$ GPa.

Although inconclusive evidence exists from shock compression experiments [64], sapphire may undergo a solid–solid phase transformation at pressures in excess of 79 GPa. Evidence of such a transformation has not been reported in indentation experiments involving twinning [32–34], though it is conceivable for such high pressures to be achieved for very sharp indenters. The possibility of such a high-pressure phase transformation in sapphire is omitted in the present phase field simulations.

4. Phase field simulations: linear theory

Simulations of wedge indentation into calcite and sapphire using the linear theory of section 2.1 are described. Numerical results are analyzed.

4.1. Boundary value problem

The problem of study is illustrated in figure 3. Simulations are two-dimensional (plane strain). A rigid, wedge-shaped indenter of angle ϕ is pressed to a depth δ into a calcite or sapphire substrate of nominal dimensions $50 \text{ nm} \times 75 \text{ nm}$. The indenter is rounded at the tip to alleviate extreme deformation that would occur with a perfectly sharp indenter; the analytical elastic

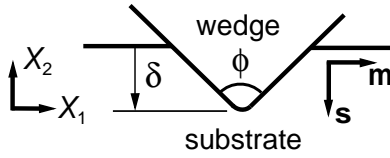


Figure 3. Wedge indentation.

solution (no twinning) for frictionless contact [38–40] indicates that the pressure immediately under the indenter tip would be infinite for a perfectly sharp indenter. Wedge angles of $\phi = 90^\circ$ and $\phi = 120^\circ$ are considered. The shear strain under the indenter is $\gamma \approx \tan(90^\circ - \phi/2)$, about 1 for the 90° wedge and about 0.58 for the 120° wedge. The substrate is rigidly bonded to the indenter along the line of contact. It is noted that this boundary condition is an idealization; in a real experiment, some slip would be expected to occur between indenter and substrate. For ductile materials and unlubricated indenters, a stick condition as considered here may be more appropriate than sliding/frictionless contact [40, 65]. The finite element software used for the simulations reported here does not presently include the capability to address multi-body contact or friction interactions. If and when such capabilities are added in the future, effects of friction coefficient on indentation can be studied.

Free boundary conditions (i.e. $t = \mathbf{0}$ and $h = 0$) are applied along the remainder of the top surface not in contact with the wedge. Recall from (20) that h is the force conjugate to variations in the order parameter; $h = 0$ is the logical boundary condition for a surface free of thermodynamic force associated with the phase field, just as $t = \mathbf{0}$ is the logical condition for a surface free of mechanical force associated with displacements. These free boundary conditions permit the order parameter and displacement to vary along the surface as an outcome of the solution. Condition $h = 0$ is also applied along the interface between indenter and substrate, which permits formation of a twin at the surface immediately beneath the indenter, as observed in experiments [1] (figure 1). Fixed boundary conditions (i.e. $\mathbf{u} = \mathbf{0}$ and $\eta = 0$ on $\partial\Omega$) are applied along the left, right and bottom sides of the substrate. Prescription of alternative conditions $h = 0$ along left, right and bottom sides did not affect the solution. The lattice orientation of the substrate in each case is such that the direction of twinning shear is parallel to the direction of indentation loading.

A initial displacement field u_2 is applied to material beneath the indenter to prevent element overlap or inversion during initial conjugate gradient iterations. A defect ($\eta = 1$) of small size (radius $\sim 5 \text{ \AA}$) underneath the indenter is typically assigned as an initial condition. When no initial defect is prescribed, twin(s) do not always nucleate in the numerical simulations. Mathematically, this phenomenon is understandable from examination of (22) and (24), which can be satisfied when $\eta = 0$ everywhere, even though the total energy of a system with a twin (i.e. with $\eta > 0$ somewhere in Ω) may be less than that in which no twinning occurs. In other words, condition $\eta = 0$ everywhere may correspond to a metastable solution. The phenomenon is also physically realistic: Garber and Stepina [8] found that twins nucleated immediately with negligible loads when surface defects were present, but required much greater indentation force to nucleate when surface defects were absent.

The numerical solution technique incorporates finite element discretization and conjugate gradient energy minimization [20]. Solutions of weak forms of equilibrium equations in section 2 are obtained, with order parameter η and displacement \mathbf{u} the nodal degrees of freedom. For the boundary conditions prescribed here, equilibrium solutions corresponds to minima of energy functional Ψ as in (42).

Table 3. Phase field simulations (linear).

Case	Material	Twin	C_{ABCD}	κ_{AB}	ϕ	Scale
1	CaCO ₃	e ⁺	Isotropic	Isotropic	90°	Nanoscale
2	CaCO ₃	e ⁺	Isotropic	Isotropic	120°	Nanoscale
3	CaCO ₃	e ⁺	Isotropic	Anisotropic	90°	Nanoscale
4	Al ₂ O ₃	B	Isotropic	Isotropic	90°	Nanoscale
5	Al ₂ O ₃	R	Isotropic	Isotropic	90°	Nanoscale
6	CaCO ₃	e ⁺	Isotropic	Isotropic	90°	Lab scale
7	Al ₂ O ₃	B	Isotropic	Isotropic	90°	Lab scale
8	Al ₂ O ₃	R	Isotropic	Isotropic	90°	Lab scale
9	CaCO ₃	e ⁺	Anisotropic	Isotropic	90°	Nanoscale
10	Al ₂ O ₃	B	Anisotropic	Isotropic	90°	Nanoscale
11	Al ₂ O ₃	B	Anisotropic	Isotropic	90°	Lab scale

Linear (i.e. three node) triangular finite elements are used, with significant mesh refinement underneath the indenter. Element size in such regions is $\sim 1 \text{ \AA}$, sufficient for resolution of gradients in order parameter at twin-parent interfaces by 10+ finite elements. Results of interest are insensitive to further increases in mesh density. Indentation depth δ is varied nominally from 0.25 nm to 4.75 nm in increments of 0.5 nm. For each increment, initial conditions are re-applied, and then the conjugate gradient algorithm is used to determine equilibrium order parameter and elastic fields.

Absolute indentation force P is computed by summing vertical nodal forces contributing to t_2 along the contact line. Absolute length L of the twin is determined by the X_2 coordinate at the tip demarcated by the local condition $\eta > 0.1$. In most cases, increasing the thickness of the substrate above 75 nm results in very little change to P or L ; any exceptions are discussed later in the context of the corresponding results.

Simulations discussed in sections 4.2 and 4.3 focus on nanometer-scale twins, i.e. nucleation phenomena. Length scales involved are in agreement with previous studies of twin nucleation [2, 20, 36, 37]. Twins modeled by Kosevich and colleagues using one-dimensional theories [1, 9, 11] are idealized with minimum thickness on the order of the interplanar spacing ($< 1 \text{ nm}$), and hence also describe nanoscopic phenomena, though the length of twins studied in such analytical models may be orders of magnitude larger. Using the present phase field approach, much larger (i.e. laboratory scale, dimensions of mm) twins can also modeled by careful scaling of the size of the indenter and substrate, the mesh density and the gradient energy parameter κ , such that the finite element mesh is able to resolve the thickness of twin boundary interfaces. This effort to model laboratory scale as opposed to nanoscale twins is described in section 4.4.

Table 3 lists simulations discussed in forthcoming parts of section 4. Solutions obtained using isotropic elasticity are grouped into cases 1–8 because these will be analyzed together later. Cases 9–11 consider anisotropic elasticity.

4.2. Isotropic elasticity

Contours of order parameter fields for cases 1, 2, 4 and 5 are shown in figure 4. The normalized indentation depth is $\Delta = 4.75$ for all cases in figure 4. Normalized (dimensionless) depth, normalized indentation force per unit out-of-plane length, and normalized twin length are defined, respectively, as

$$\Delta = \frac{\delta}{l}, \quad \Pi = \frac{P}{\hat{E}l}, \quad \Lambda = \frac{L}{l}. \quad (49)$$

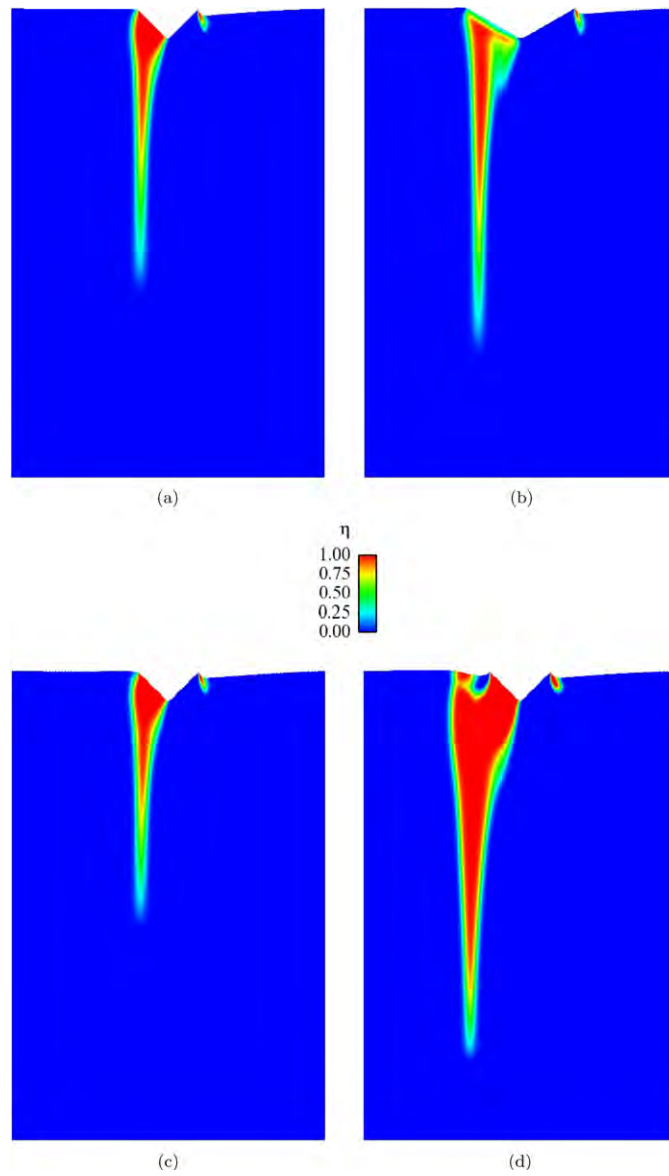


Figure 4. Order parameter η field for isotropic elastic solutions at the nanoscale at indentation depth $\Delta = 4.75$: (a) case 1: calcite, e^+ twin, 90° wedge. (b) Case 2: calcite, e^+ twin, 120° wedge. (c) Case 4: sapphire, B twin, 90° wedge. (d) Case 5: sapphire, R twin, 90° wedge.

Effective Young's modulus \hat{E} , Young's modulus E and Poisson's ratio ν are

$$\hat{E} = \frac{E}{1 - \nu^2}, \quad E = \frac{\mu(3\lambda + 2\mu)}{\lambda + \mu}, \quad \nu = \frac{\lambda}{2(\lambda + \mu)}. \quad (50)$$

The definition of \hat{E} is motivated by the analytical linear elastic solution (with no twinning and frictionless contact) [38–40], wherein the mean contact pressure between indenter and substrate is $p_m = \hat{E} \cot(\phi/2)$.

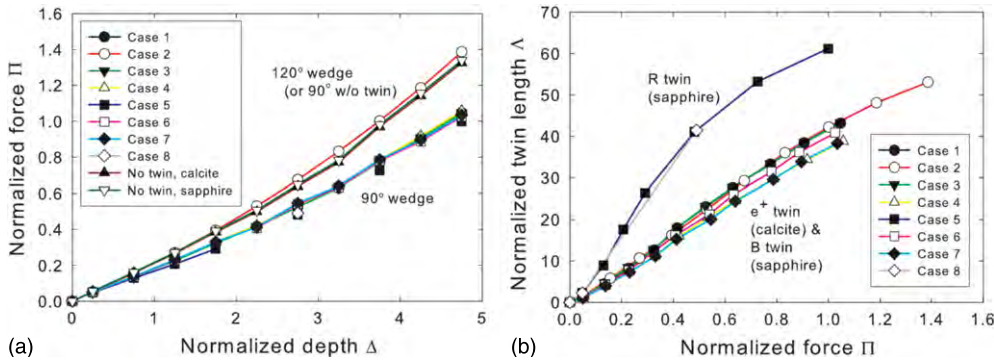


Figure 5. Normalized indentation force versus indentation depth (a) and normalized twin length versus force (b) for isotropic elastic constants.

In each case, a primary twin forms under the left side of the indenter, where the driving shear stress for twinning τ of (23) is positive in sign. Directly under the right side of the wedge, τ is negative in sign, since the shear strain is directed in the anti-twinning sense with respect to the orientation of the twin system. The sharp tip predicted for e^+ twinning in calcite agrees with observations from indentation experiments conducted from the 1930s to the 1970s [1, 5, 8, 11]. Long, lenticular-shaped micro-twins in indentation of sapphire have been reported [32]. The predicted sharp tip also verifies that described by the early analytical solution of Lifshitz [12].

Also noteworthy are the secondary twins that form at the edge of the indenter (right side) where the shear deformation is directed in the twinning (as opposed to anti-twinning) sense. This phenomenon is reminiscent of the appearance of twins near the outer edge of spherical indenters reported by Garber and Stepina [8].

Comparing figure 4(a) with figure 4(b), a longer twin is produced in calcite, for the same Δ , when an indenter with larger wedge angle is used. Comparing figure 4(c) with figure 4(d), for the same Δ , a rhombohedral (R) twin is significantly longer than a corresponding basal (B) twin in sapphire. Recall from table 2 that the shear γ_0 for B twinning is larger than that for R twinning (0.635 versus 0.202) as is the surface energy Γ (745 versus 125 mJ m⁻²). The twinning shear for calcite is 0.694 (table 1). Comparing figure 4(a) with figures 4(c) and (d), for the same Δ and wedge angle, e^+ twins in calcite and B twins in sapphire are much closer in length and appearance than are R twins in sapphire. It is suggested that larger/longer R twins are required to achieve comparable relaxation in elastic strain energy than B twins because of the smaller stress-free shear γ_0 in the former.

Another interesting feature in figure 4(b) is the thin boundary layer at the surface of contact under the left side of the wedge where $\eta < 1$. This layer appears because the imposed shear strain directly under the 120° indenter is about 0.58, which is less than the transformation shear 0.694 for calcite. On the other hand, for indentation by 90° wedges, the imposed shear strain is about 1, which is greater than γ_0 , and hence complete transformation with $\eta = 1$ is energetically favorable along the contact boundaries under the left sides of the 90° wedges.

Indentation force versus depth is shown in figure 5(a) for cases 1–8, along with force versus depth for pure elastic solutions (i.e. no twinning). Results for no twinning are obtained for 90° wedges. Twinning induces a significant reduction in force relative to pure elasticity. Use of a 120° wedge (case 2) rather than a 90° wedge produces a larger force because of the former's larger contact area. In figure 5(a), force-versus-depth data for 90° wedge indentation with twinning collapse to nearly the same curve when normalized to dimensionless form by the appropriate quantities via (49).

Twin length versus indentation force is shown in figure 5(b). In all cases, twin length increases monotonically with increasing force or with increasing depth of indentation. Behavior is similar for e^+ twinning in calcite and B twinning in sapphire. On the other hand, R twins in sapphire are significantly longer under the same normalized force. It was found that for twin lengths $\Lambda \lesssim 50$, interaction with the rigid lower boundary $\partial\Omega$ of the domain does not affect the twin length (recall $\eta = 0$ is imposed on $X_2 = 0$). For the R twin, the two data points corresponding to the largest values of Λ indicate some influence of the lower boundary, which tends to repel and hence shorten the twin. Perhaps most noteworthy from figure 5(b), for e^+ twinning in calcite and B twinning in sapphire, twin length versus force for wedge indentation reduce to nearly the same curve when normalized via (49).

It was remarked in section 3.1 that the choice of anisotropic surface energy in (43) might facilitate more elongated or sharper twins, as was observed for the problem of homogeneous twin nucleation in previous work [20]. Comparing cases 1 and 3, use of anisotropic surface energy in (43) with energy per unit area differing by a factor of ≈ 2 in directions parallel and perpendicular to the habit plane results in negligible differences in force and length, and contours of η are also negligible between cases 1 and 3 (not shown). Thus, the present results suggest that anisotropic surface energy does not significantly affect predicted twin morphology during wedge indentation, at least for the materials and ranges of physical parameters considered here.

4.3. Anisotropic elasticity

Contours of order parameter η are compared for anisotropic and isotropic elastic constants in figure 6. Shown are results for 90° wedges at an indentation depth of $\Delta = 4.75$. Qualitatively, with regards to twin shape, predictions of anisotropic and isotropic models agree. Use of anisotropic elasticity produces a somewhat shorter e^+ twin in calcite than does the corresponding isotropic model (figures 6(a) and (b)). Use of anisotropic elasticity produces a slightly longer B twin in sapphire than does the corresponding isotropic model (figures 6(c) and (d)). Recall from section 3 that elastic anisotropy (in terms of ratios of elastic constants) is significantly greater in calcite than sapphire; however, relative influences of anisotropy on the indentation solutions might also be influenced by other factors such as differences in twinning shear γ_0 and different surface energies prescribed for the two materials.

Normalized indentation force versus indentation depth for 90° wedge indentation is shown in figure 7(a) for e^+ twinning in calcite and B twinning in sapphire. All curves except that for anisotropic calcite coincide; the indentation force tends to be lower in the latter. Normalized twin length versus indentation force are shown in figure 7(b), again for e^+ twinning in calcite and B twinning in sapphire. All results collapse to nearly the same monotonically increasing (and nearly linear) relationship.

4.4. Scaling to laboratory dimensions

Modeling twin nucleation and growth at dimensions of millimeters or larger, i.e. at laboratory scales corresponding to traditional indentation experiments [1, 5, 8, 11], is not feasible without proper scaling of the interfacial thickness. Resolution of an interface of thickness l of 1 nm, as considered in nanoscale simulations discussed in sections 4.2 and 4.3, requires a numerical discretization with finite elements of size on the order of 1 Å; discretization of a domain of 1 cm² would require $\sim 10^{16}$ such elements, for example. In phase field calculations, the pragmatic idea of treating the interface as having an adjustable or scalable thickness has been used often for modeling larger systems [23, 24]. Following such an approach, here the equilibrium

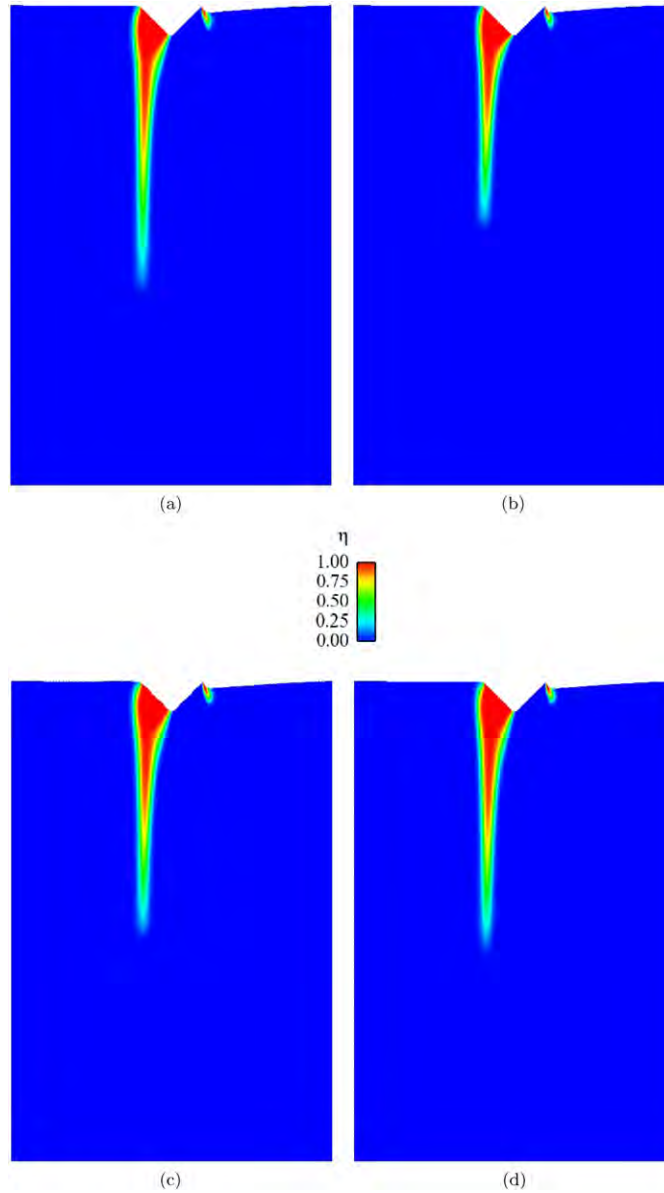


Figure 6. Order parameter η field for isotropic and anisotropic elastic solutions at the nanoscale at indentation depth $\Delta = 4.75$ with 90° wedge: (a) case 1: calcite, e^+ twin, isotropic elasticity. (b) Case 9: calcite, e^+ twin, anisotropic elasticity. (c) Case 2: sapphire, B twin, isotropic elasticity. (d) Case 10: sapphire, B twin, anisotropic elasticity.

interfacial thickness is scaled to $l = 1$ mm, an increase by a factor of 10^6 above the value of 1 nm used in sections 4.2 and 4.3. In other words, in the scaled model, the equilibrium width of the twin boundary is ≈ 1 mm. Recall that 1 nm corresponds to a distance over which atoms deviate from their ideal positions in atomic simulations of twin boundaries [22].

To achieve the desired scaling $l \rightarrow Fl$, values of constants in (17) are adjusted as

$$\kappa \rightarrow F^2 \kappa, \quad A \rightarrow A, \quad (51)$$

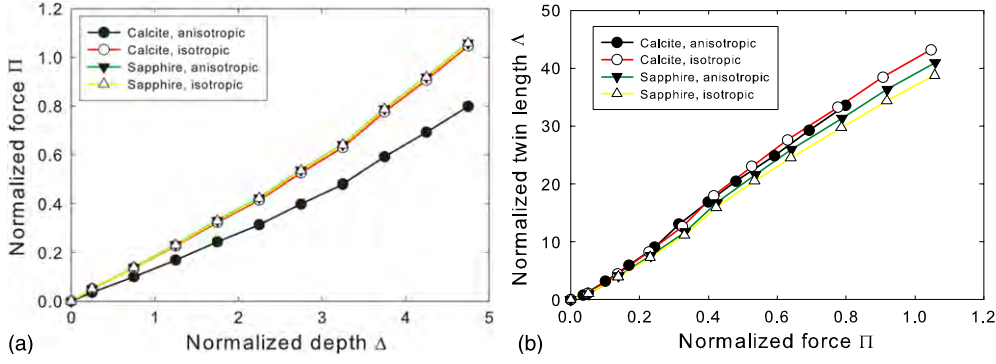


Figure 7. Normalized indentation force versus indentation depth (a) and normalized twin length versus force (b) for e^+ twins in calcite and B twins in sapphire.

where in this particular case, $F = 10^6$. The transformation in (51) preserves the ratio of interfacial energy to strain energy on a per-unit-volume basis; W of (8) and f_0 of (16) are unchanged:

$$W \rightarrow W, \quad f_0 \rightarrow f_0. \quad (52)$$

The gradient contribution to interfacial energy per unit volume f in (15) is also unchanged since

$$\nabla \rightarrow \nabla/F, \quad \kappa|\nabla\eta|^2 \rightarrow (F^2\kappa)|(\nabla\eta/F)|^2 = \kappa|\nabla\eta|^2. \quad (53)$$

In laboratory (millimeter) scale simulations discussed next, room temperature (as opposed to 0 K) elastic constants are used, to better mimic ambient test conditions.

Representative results are compared in contour plots of η in figure 8. In figure 8(a), nanoscale results are shown, and absolute substrate dimensions are $50 \text{ nm} \times 75 \text{ nm}$. In figure 8(b), laboratory scale results with parameters modified via (51) are shown, and dimensions are $50 \text{ mm} \times 75 \text{ mm}$. Close similarity between cases 1 and 6 in figures 8(a) and (b) (calcite, e^+ twin, isotropic elasticity) demonstrates the ability of the scaling to produce self-similar results for linear elasticity. Differences in twin length between figures 8(a) and (b) are a consequence of the increase in compliance of the elastic constants at room temperature relative to 0 K. As shown in figure 5, data for indentation force versus depth and twin length versus indentation force are nearly identical when normalized to dimensionless form. For example, compare results for cases 1 and 6 (calcite) and cases 4 and 7 (sapphire, B twin). Close similarity between cases 10 and 11 (sapphire, B twin, anisotropic elasticity) demonstrates the ability of the scaling procedure to produce self-similar results for anisotropic elasticity.

Limitations of the above scaling method should be noted. Per unit volume, the ratio of interfacial energy to strain energy is maintained by the scaling procedure: both W and f entering (7) are unchanged by the scaling. This explains why solutions obtained by energy minimization appear nearly identical in figure 8: the same problem (with different units) is essentially solved in each case. However, per unit area, energy associated with the interface is increased by a factor of F . Interfacial energy per unit volume is energy per unit area divided by thickness. Because interfacial thickness is increased by a substantial factor (i.e. F), small features cannot be resolved in absolute dimensions.

The present model predictions would benefit from quantitative comparisons with experiments. Such comparisons are presently inhibited by limitations in reporting of experimental geometry and data. Regarding the former, it is typically stated that a ‘knife edge’,

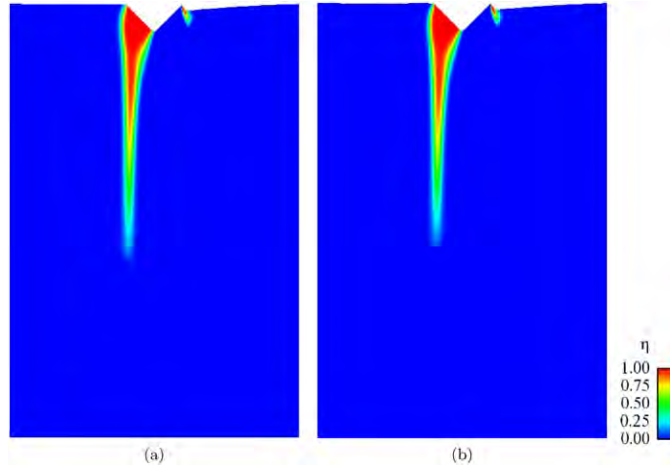


Figure 8. Order parameter η field for solutions at nanometer and millimeter scales at indentation depth $\Delta = 4.75$ with 90° wedge: (a) case 1: calcite, e^+ twin, isotropic elasticity, $l = 1$ nm. (b) Case 6: calcite, e^+ twin, isotropic elasticity, $l = 1$ mm.

‘chisel’, or ‘wedge’ is used to produce an elastic twin in calcite, but the wedge angle (i.e. ϕ of figure 3) is not reported [1, 9, 7, 11]. Results of measurements of force versus twin length are given only implicitly as parameters entering dislocation models [9, 11]; raw force versus length data enabling comparison with the present predictions are apparently unpublished. Data are available for spherical indentation of calcite [6]; however twinning under spherical indentation requires 3D modeling outside the scope of this work. New experiments studying effects of wedge angles as reported in detail for other elastic and plastic materials [39] would be useful. It is reiterated that predictions reported here do agree qualitatively with experimental observations: a long thin twin forms under one side of the indenter, the twin tip is sharp, and the twin length increases with increasing applied load.

5. Phase field simulations: nonlinear theory

Simulations of indentation using the nonlinear theory of section 2.2 are described; numerical results are analyzed and compared with those from the linear theory.

5.1. Boundary value problem

The same indentation boundary value problems described in section 4 are considered here in the context of the finite strain model of section 2.2. The numerical solution technique incorporates procedures nearly identical to those discussed in section 4.1. Solutions of weak forms of the equilibrium equations in section 2.2 are obtained, with order parameter η and displacement $\mathbf{u} = \boldsymbol{\chi} - \mathbf{X}$ the nodal degrees of freedom. For the boundary conditions prescribed here, the equilibrium solution corresponds to a minima of energy functional Ψ as in (42). In a few exceptional cases involving large indentation depths in sapphire, converged solutions could not be obtained for all increments; in those cases, solution data shown in subsequent figures is necessarily limited to that available from converged solutions. For simulations incorporating the geometrically nonlinear neo-Hookean model, it was found that accelerated convergence towards equilibrium solutions could often be obtained by using the corresponding linear elastic

Table 4. Phase field simulations (nonlinear and linear).

Case	Material	Twin	Model	ϕ	Scale
1	CaCO ₃	e ⁺	Nonlinear	90°	Nanoscale
2	CaCO ₃	e ⁺	Linear	90°	Nanoscale
3	Al ₂ O ₃	B	Nonlinear	90°	Nanoscale
4	Al ₂ O ₃	B	Linear	90°	Nanoscale
5	Al ₂ O ₃	R	Nonlinear	90°	Nanoscale
6	Al ₂ O ₃	R	Linear	90°	Nanoscale
7	CaCO ₃	e ⁺	Nonlinear	120°	Nanoscale
8	CaCO ₃	e ⁺	Linear	120°	Nanoscale
9	Al ₂ O ₃	B	Nonlinear	90°	Lab scale
10	Al ₂ O ₃	B	Linear	90°	Lab scale

phase field solutions reported in section 4 as an initial guess. This initialization procedure was used to obtain many of the nonlinear phase field solutions discussed later involving relatively large indentation depths. It was found that the same final equilibrium solution was obtained using this initialization method or the initial conditions described in section 4.1.

Simulations discussed in sections 5.2 and 5.3 focus on nanometer-scale twins, i.e. nucleation phenomena, arising from indenters with respective wedge angles of $\phi = 90^\circ$ and $\phi = 120^\circ$. Length scales involved (i.e. tens of nm) are similar to those of prior analytical and computational studies of twin nucleation [2, 20, 36, 37]. Results of modeling laboratory scale as opposed to nanoscale twins are presented in section 5.4.

Table 4 lists simulations discussed in section 5. Calcite (e⁺ twin system) and sapphire (B and R twin systems) are modeled. Odd-numbered simulation cases incorporate the geometrically nonlinear phase field model with neo-Hookean elasticity of section 2.2. Even-numbered cases incorporate the geometrically linear, linear elastic phase field model of section 2.1. For a given nonlinear solution, the linear solution for the same material and boundary conditions corresponds to the subsequent case number in table 4.

5.2. Nano-indentation with 90° wedge

Contours of order parameter and shear stress fields in calcite for simulation cases 1 (nonlinear theory) and 2 (linear theory) are shown in figure 9. The normalized indentation depth is $\Delta = 4.75$. Normalized (dimensionless) depth, normalized indentation force and normalized twin length are defined, respectively, as in (49).

For each case in figure 9, a primary twin forms under the left side of the indenter, where the driving shear stress for twinning τ of (41) is positive in sign. Under the right side of the wedge, τ is negative in sign, since the shear strain is directed in the anti-twinning sense with respect to the orientation of the twin system. A secondary twin arises at the edge of the indenter at the free surface (right side) where the shear deformation is directed in the twinning (as opposed to anti-twinning) sense.

For purposes of comparison, contour legends for the order parameter in these and subsequent figures are restricted to $\eta \in [0, 1]$. Occasionally, values of η slightly exceeded unity at one or a few nodes immediately under the indenter. The current numerical implementation of the phase field model places no hard bounds on η ; values $\eta < 0$ are set to 0 in (5), while values $\eta > 1$ are set to 1 in (5). Thus, values outside the range [0,1] offer no advantage with regards to minimization of elastic strain energy, and are penalized in the double-well potential (16).

Comparing figure 9(a) with figure 9(b), order parameter contours and twin lengths are similar for nonlinear and linear models in this instance. One minor difference arises: in the

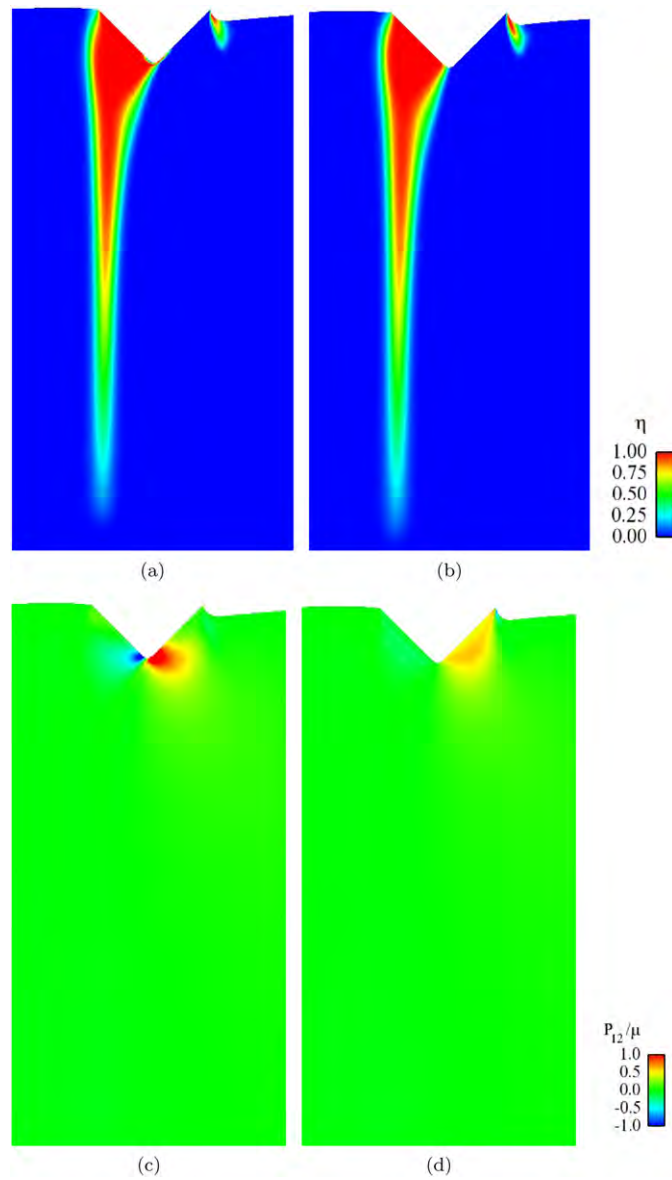


Figure 9. Close-up contours of order parameter and shear stress for nano-indentation with 90° wedge at depth $\Delta = 4.75$: (a) η , case 1: calcite, e^+ twin, nonlinear theory. (b) η , Case 2: calcite, e^+ twin, linear theory. (c) P_{12}/μ , Case 1: calcite, e^+ twin, nonlinear theory. (d) P_{12}/μ , Case 2: calcite, e^+ twin, linear theory.

nonlinear solution (figure 9(a)), a thin layer of twinned material ($\eta \approx 1$) emerges under the right side of the indenter, near the tip. Such a layer is absent in the linear solution of figure 9(b). Shear stress contours in figures 9(c) and (d) differ substantially for nonlinear and linear models. The shear stress is more severe, and more strongly concentrated under the tip of the indenter, for the nonlinear model (figure 9(c)) than the linear model (figure 9(d)). Maximum shear stresses can be large, with local magnitudes exceeding the shear modulus for results of the nonlinear theory.

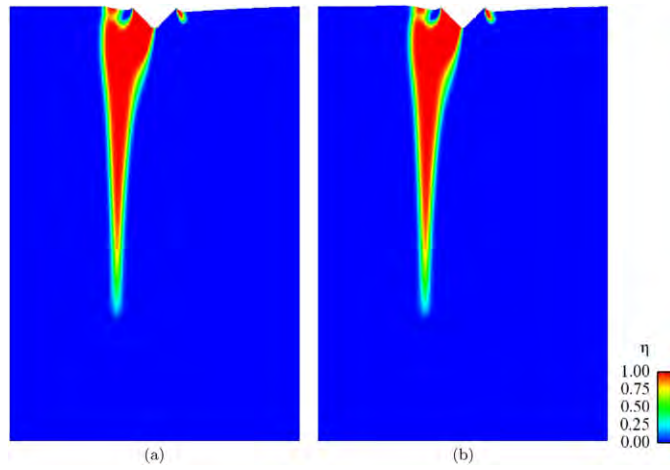


Figure 10. Order parameter η field for nano-indentation of sapphire to depth of $\Delta = 3.75$ with 90° wedge: (a) Case 5: sapphire, R twin, nonlinear theory (b) Case 6: sapphire, R twin, linear theory.

Contours of order parameter fields for indentation of sapphire, cases 5 (nonlinear, R twin) and 6 (linear, R twin) are shown in figure 10. Order parameter contours and twin lengths are similar for nonlinear and linear models. In the nonlinear solution, a thin layer of twinned material ($\eta \approx 1$) again emerges under the right side of the indenter, near the tip, while such a layer is absent in the corresponding linear solution.

For the same indentation depth Δ , a rhombohedral (R) twin is predicted to be significantly longer than a corresponding basal (B) twin in sapphire. Recall from table 2 that the shear γ_0 for B twinning is larger than that for R twinning (0.635 versus 0.202) as is the surface energy Γ (745 versus 125 mJ m^{-2}). Longer R twins may be required to achieve comparable relaxation in elastic strain energy than B twins because of the smaller stress-free shear γ_0 in the former. This trend (R twins longer than B twins) was consistent among results of both linear and nonlinear models.

Indentation force versus depth is shown in figure 11(a) for cases 1–6. Force versus depth data for 90° wedge indentation, when normalized by the appropriate quantities via (49), are similar for all cases at small indentation depths ($\Delta \lesssim 2.5$). At larger indentation depths, indentation forces for nonlinear models (cases 1, 3 and 5) exceed forces for corresponding linear models (cases 2, 4 and 6). Such differences result, in part, from the increase in tangent stiffness (e.g. bulk modulus) with increasing compressive pressure in the neo-Hookean elasticity model. For e^+ twinning in calcite and B twinning in sapphire, the indentation force in the nonlinear model (case 1 or 3) only modestly exceeds that for the complementary linear model (case 2 or 4) at $\Delta \gtrsim 2.5$. The indentation force increases dramatically for case 5 (sapphire, R twin) at larger indentation depths relative to the force for the corresponding linear model (case 6). Order parameter (figure 10) and displacement fields demonstrate little differences among linear and nonlinear solutions at large indentation depths, whereas local compressive stress magnitudes become comparatively much larger for the nonlinear model. It is suggested that the increase in force in the nonlinear model is a result of nonlinear elastic contributions to stress (especially pressure) that become stronger at larger indentation depths and for larger R twins.

Twin length versus indentation force is shown in figure 11(b). In all cases, twin length increases monotonically with increasing force or with increasing depth of indentation. Behavior is quantitatively similar for e^+ twinning in calcite and B twinning in sapphire. R twins

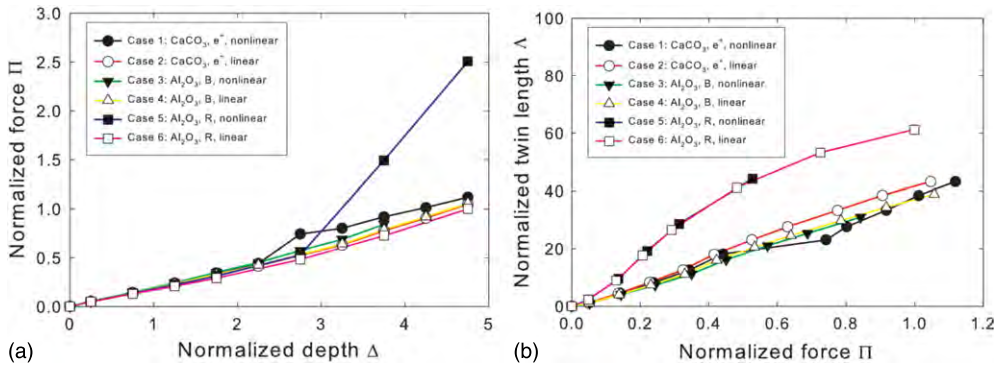


Figure 11. Normalized indentation force versus indentation depth (a) and normalized twin length versus force (b) for cases 1–6.

in sapphire are significantly longer under the same normalized force. From figure 11(b), for e^+ twinning in calcite and B twinning in sapphire, twin length versus indentation force data normalized by (49) reduce to similar curves.

5.3. Nano-indentation with 120° wedge

Contours of order parameter field η for cases 7 (calcite, nonlinear theory) and 8 (calcite, linear theory) for indentation with a 120° wedge are shown in figure 12 for indentation depths of $\Delta = 3.75$ (figures 12(a) and (b)) and $\Delta = 4.75$ (figure 12(c) and (d)). At each depth, the absolute length of the long, thin primary twin is nearly identical for nonlinear and linear models. The sharp tip predicted for e^+ twinning in calcite agrees with observations from indentation experiments [1, 5, 8, 11].

Predicted twin morphologies are strikingly different for nonlinear and linear models. For the linear theory, a single continuous primary twin forms under the left side of the indenter. For the nonlinear theory, a layered twin structure with alternating regions of large and small values of η forms under the left side of the indenter. The number of horizontal layers increases with increasing indentation depth: e.g. two horizontal layers are evident in figure 12(a) and three arise in figure 12(c). Such layered structures were not reported in early experimental work on indentation of calcite from the 1930s to the 1970s [1, 5, 8, 11]; however, such microstructures may simply have not been detectable by the optical/photographic equipment available at that time. Kaga and Gilman [10] observed layered (lamellar) structures in twinned calcite specimens through etch pit studies. It was suggested that etch pit lines could be associated with positions where a twin boundary interface temporarily rested during growth of a twin [10]. The alternating layers of twinned crystal under the indenter evident in the nonlinear results in figure 12 are reminiscent of the finely twinned energy-minimizing structures in theories of martensitic phase transformations [27, 29]. Because of the energetic penalty incurred by boundary regions of $\eta \neq 0, 1$ in the phase field theory, the layered structures that emerge in the nonlinear theory must offer a substantial reduction in elastic strain energy relative to a solution in which a single continuous primary twin forms, as in the linear theory.

Other phase field simulations incorporating geometrically linear, but possibly anisotropic, elasticity have predicted layered structures of twin domains in the context of martensitic transformations [46, 47]. An anisotropic linear elastic–plastic finite element study [66] showed that local shear stress distributions favor formation of lenticular shaped twins, and that above a

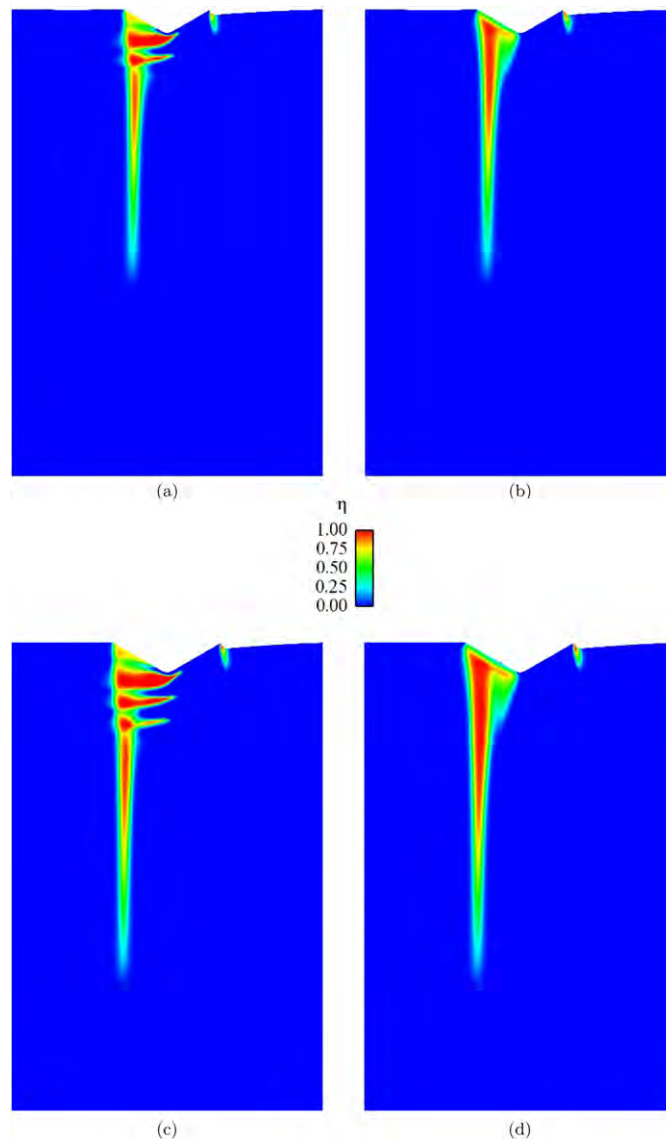


Figure 12. Order parameter η field for nano-indentation with 120° wedge: (a) case 7: calcite, e^+ twin, $\Delta = 3.75$, nonlinear theory. (b) Case 8: calcite, e^+ twin, $\Delta = 3.75$, linear theory. (c) Case 7: calcite, e^+ twin, $\Delta = 4.75$, nonlinear theory. (d) Case 8: calcite, e^+ twin, $\Delta = 4.75$, linear theory.

threshold twinned volume fraction, formation of a layered microstructure consisting of multiple twins is energetically favorable to formation of a single large twin. Reported finite element calculations did not account for surface energy, which was noted would become important for very small twins in the nucleation stage [66]. None of these other works addressed indentation loading.

In all cases shown in figure 12, a thin boundary layer arises at the surface of contact under the left side of the wedge, where $\eta < 1$. This layer appears because the imposed shear strain directly under the 120° indenter is about 0.58, which is less than the transformation shear

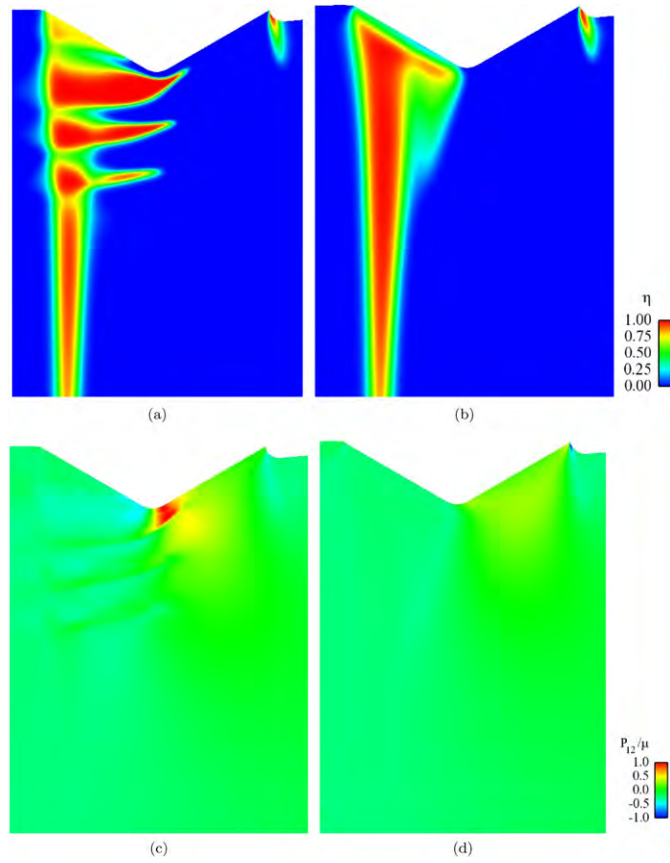


Figure 13. Close-up contours of order parameter and shear stress for nano-indentation with 120° wedge at depth $\Delta = 4.75$: (a) η , case 7: calcite, e^+ twin, nonlinear theory. (b) η , Case 8: calcite, e^+ twin, linear theory. (c) P_{12}/μ , Case 7: calcite, e^+ twin, nonlinear theory. (d) P_{12}/μ , Case 8: calcite, e^+ twin, linear theory.

0.694 for calcite. On the other hand, for indentation by 90° wedges discussed in section 5.2 (figure 9), the imposed shear strain is about 1, which is greater than γ_0 , and hence complete transformation with $\eta = 1$ is energetically favorable along the contact boundaries under the left sides of 90° wedges. Because the layered twin structure of the nonlinear theory does not emerge in simulations of indentation by 90° wedges, the appearance of such layers for indentation by 120° wedges (imposed shear of $0.58 < \gamma_0 = 0.694$) could be explained by similar arguments.

Close-up views of order parameter η and shear stress component P_{12} are shown in figure 13 for cases 7 and 8. Shear stress contours in figures 13(c) and (d) differ substantially for nonlinear and linear models. As was observed in figure 9, the shear stress is more severe, and more strongly concentrated under the tip of the indenter, for the nonlinear model (figure 13(c)) than the linear model (figure 13(d)). Alternating layers of shear stress that accompany the lamellar twin structure predicted by the nonlinear theory are just visible in figure 13(c).

Indentation force versus depth is shown in figure 14(a) for cases 7–10. Twin length versus indentation force is shown in figure 14(b). Results for cases 7 and 8 are discussed here; cases 9 and 10 are discussed in section 5.4. Force-versus-depth data for 120° wedge indentation,

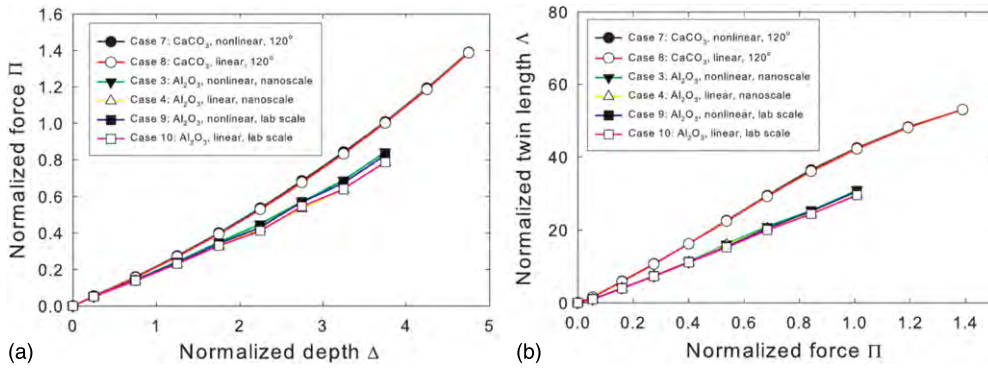


Figure 14. Normalized indentation force versus indentation depth (a) and normalized twin length versus force (b) for cases 3, 4 and 7–10.

when normalized by (49), are almost identical for linear and nonlinear models. Indentation force and twin length predicted by nonlinear theory exceed corresponding values predicted by linear theory by less than 1%. Twin length increases monotonically with increasing force or with increasing depth of indentation.

5.4. Scaling to laboratory dimensions

For scaling according to the transformation $l \rightarrow Fl$, values of constants in (17) are adjusted as in (51) of section 4.4. Again, for the present problem, $F = 10^6$, scaling the interface thickness from 1 nm to 1 mm. In laboratory (millimeter) scale simulations discussed next, room temperature (as opposed to 0 K) elastic constants are used, to better represent ambient experimental conditions [1, 5, 8, 11].

Representative results are compared for nonlinear and linear theories in contour plots of η in figure 15, corresponding to basal twins in sapphire induced by 90° wedge indentation. Figures 15(a) and (b) can be compared with nanoscale results in figures 6(c) and (d), though the indentation depth is slightly smaller in the former. In figures 6(c) and (d), nanoscale results are shown, and the absolute substrate dimensions are $50 \text{ nm} \times 75 \text{ nm}$. In figures 15(a) and (b), laboratory scale results with parameters scaled via (51) are shown, and the dimensions are $50 \text{ mm} \times 75 \text{ mm}$. Note that twin morphologies are similar for model predictions at each length scale. Linear and nonlinear theories also predict similar order parameter profiles in figure 15. Similar to what was observed in figure 9(a), only in the nonlinear solution does a thin layer of twinned material ($\eta \approx 1$) emerge under the right side of the indenter near the tip.

Indentation force versus depth is shown in figure 14(a); twin length versus indentation force is shown in figure 14(b). Force-versus-depth data for 90° wedge indentation of sapphire with B twins, when normalized by the appropriate quantities via (49), is quantitatively very similar for linear and nonlinear models at both the nanoscale and laboratory scale (cases 3, 4, 9, and 10). Normalized twin length data for linear and nonlinear models at each length scale also collapse to nearly the same monotonically increasing curve, as demonstrated by the nearly indistinguishable results for sapphire in figure 14(b). Close similarity among results for cases 3 and 9 in figure 14 demonstrates the ability of the scaling method of section 4.4 to produce geometrically self-similar results for nm- and mm-sized specimens using the nonlinear theory.

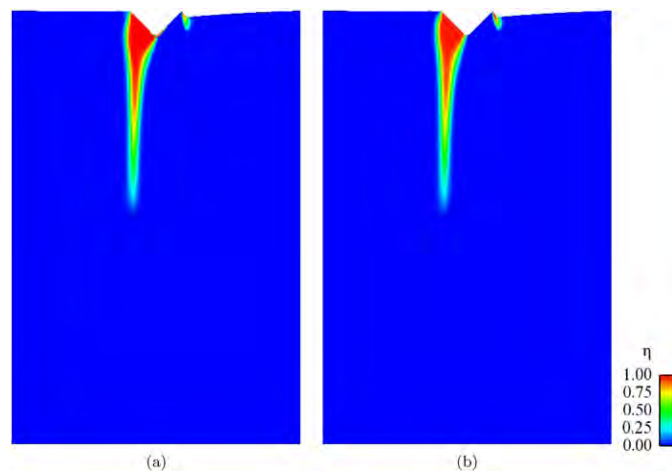


Figure 15. Order parameter η field for laboratory (mm) scale indentation with 90° wedge at depth $\Delta = 4.25$: (a) case 9: sapphire, B twin, nonlinear theory. (b) Case 10: sapphire, B twin, linear theory.

6. Conclusions

A phase field model for twinning in elastic crystals has been developed and exercised for the problem of indentation with wedges. Two transparent materials have been studied: calcite and sapphire. Predictions of nonlinear (i.e. finite strain) theory have been compared with those of geometrically linear theory.

Phase field predictions of indentation agree qualitatively with experimental observations: a long thin twin forms asymmetrically beneath one side of the indenter, the tip of the twin is sharp and the length of the twin increases with increasing force. Normalized, dimensionless variables for indentation depth, indentation force, and twin length have been derived. It is emphasized that physically realistic twin shapes are predicted by a model whose only parameters are the elastic constants, twin boundary energy, and twin boundary thickness, all of which can be obtained from independent experiments or quantum/molecular mechanics calculations.

Qualitatively similar twin shapes have been obtained using isotropic and anisotropic elastic constants. The difference in predicted twin length between isotropic and anisotropic models is greater in sapphire than in calcite. Basal and rhombohedral twins have been studied in sapphire: predicted rhombohedral twins are longer than basal twins for the same indentation force. Use of anisotropic rather than isotropic surface energy has little effect on twin morphology or indentation force for the particular indentation boundary conditions and ranges of material parameters considered here.

A scaling method has been developed for modeling behavior of specimens of (mm-to-cm) sizes on the order of those studied experimentally in traditional indentation, as opposed to nano-indentation. Nearly identical twin morphologies are obtained for nanometer-scale specimens and millimeter (lab) scale specimens. Twin length versus indentation force data, when properly normalized to dimensionless form, collapse to nearly the same monotonically increasing curve for e^+ twins in calcite and basal twins in sapphire, for nm- and mm-scale simulations, and for 90° and 120° wedges.

Indentation forces are greater in the nonlinear model than the linear model because of the decreasing elastic compliance with increasing pressure in nonlinear model. Normalized

relationships between twin length and indentation force are similar for linear and nonlinear theories at both nanometer and millimeter scales. Twin morphologies are similar for linear and nonlinear theories for indentation with 90° wedges: in each case, a single, continuous primary twin forms under one side of the indenter, and a small secondary twin forms at the free surface at the opposite edge. Perhaps most interestingly, in the nonlinear model, indentation of calcite with a 120° wedge produces a lamellar twin structure between the indenter and the long sharp primary twin. The number of twin lamellae increases with increasing indentation depth. This complex, layered microstructure is not predicted by the linear theory, which instead predicts a single continuous primary twin.

Acknowledgments

Dr M A Grinfeld (US ARL) is acknowledged for suggesting study of the problem of elastic twinning in calcite and for providing insight into relevant historical references.

References

- [1] Kosevich A M and Boiko V S 1971 Dislocation theory of the elastic twinning of crystals *Sov. Phys.—Usp.* **14** 286–316
- [2] Christian J W and Mahajan S 1995 Deformation twinning *Prog. Mater. Sci.* **39** 1–157
- [3] Clayton J D 2011 *Nonlinear Mechanics of Crystals* (Dordrecht: Springer)
- [4] Hirth J P and Lothe J 1982 *Theory of Dislocations* (New York: Wiley) 2nd edn
- [5] Garber R I 1938 *Dokl. Akad. Nauk SSSR* **21** 233
- [6] Obreimov I V and Startsev V I 1959 Work of formation of an elastic twin in calcite *Sov. Phys.—JETP* **35** 743–8
- [7] Cooper R E 1962 Kinetics of elastic twinning in calcite *Proc. R. Soc. Lond. A* **270** 525–37
- [8] Garber R I and Stepina E I 1965 Rules governing the motion of dislocations during deformation twinning *Sov. Phys. Solid State* **5** 152–8
- [9] Boiko V S and Garber R I 1966 Determination of the phenomenological dislocation theory parameters for elastic twins in calcite *Sov. Phys.—JETP* **23** 602–5
- [10] Kaga H and Gilman J J 1969 Twinning and detwinning in calcite *J. Appl. Phys.* **40** 3196–207
- [11] Boiko V S, Garber R I and Kosevich A M 1994 *Reversible Crystal Plasticity* (New York: AIP)
- [12] Lifshitz I M 1948 Macroscopic description of the phenomenon of crystal twinning *Zh. Eksp. Teor. Fiz.* **18** 1134–43
- [13] Peierls R E 1940 The size of a dislocation *Proc. Phys. Soc.* **52** 34–7
- [14] Tomé C N, Wenk H-R, Canova G R and Kocks U F 1991 Simulations of texture development in calcite: comparison of polycrystal plasticity theories *J. Geophys. Res.* **96** 11865–75
- [15] Barton N R and Wenk H R 2007 Dauphiné twinning in polycrystalline quartz *Mod. Sim. Mater. Sci. Eng.* **15** 369–84
- [16] Clayton J D 2009 A continuum description of nonlinear elasticity, slip, and twinning, with application to sapphire *Proc. R. Soc. Lond. A* **465** 307–34
- [17] Proust G, Tomé C N, Jain A and Agnew S R 2009 Modeling the effect of twinning and detwinning during strain-path changes of magnesium alloy AZ31 *Int. J. Plasticity* **25** 861–80
- [18] Clayton J D 2010 Modeling finite deformations in trigonal ceramic crystals with lattice defects *Int. J. Plasticity* **26** 1357–86
- [19] Barton N R, Bernier J V and Edmiston J K 2009 Bringing together computational and experimental capabilities at the crystal scale *Shock Compression of Condensed Matter* ed M Elert *et al AIP Conf. Proc.* **1195** 73–8
- [20] Clayton J D and Knap J 2011 A phase field model of deformation twinning: nonlinear theory and numerical simulation *Physica D* **240** 841–58
- [21] Dandekar D P and Ruoff A L 1968 Temperature dependence of the elastic constants of calcite between 160° and 300° K *J. Appl. Phys.* **39** 6004–9
- [22] Bruno M, Massaro F R, Rubbo M, Prencipe M and Aquilano D 2010 (10.4), (01.8), (01.2), and (00.1) twin laws of calcite CaCO_3 : equilibrium geometry of the twin boundary interfaces and twinning energy *J. Cryst. Growth Des.* **10** 3102–9
- [23] Emmerich H 2003 *The Diffuse Interface Approach in Materials Science: Thermodynamic Concepts and Applications of Phase-field Models* (Berlin: Springer)

- [24] Steinbach I 2009 Phase-field models in materials science *Modelling Simul. Mater. Sci. Eng.* **17** 073001
- [25] Grinfeld M A 1980 Conditions for thermodynamic phase equilibrium in a nonlinear elastic material *Dokl. Akad. Nauk SSSR* **251** 10–4
- [26] James R D 1981 Finite deformation by mechanical twinning *Arch. Ration. Mech. Anal.* **77** 143–76
- [27] Ball J M and James R D 1987 Fine phase mixtures as minimizers of energy *Arch. Ration. Mech. Anal.* **100** 13–52
- [28] Grinfeld M A 1991 *Thermodynamic Methods in the Theory of Heterogeneous Systems* (Sussex: Longman)
- [29] Bhattacharya K 1993 Comparison of the geometrically nonlinear and linear theories of martensitic transformation *Cont. Mech. Thermodyn.* **5** 205–42
- [30] Kronberg M L 1957 Plastic deformation of single crystals of sapphire: basal slip and twinning *Acta Metall.* **5** 507–24
- [31] Heuer A H 1966 Deformation twinning in corundum *Phil. Mag.* **13** 379–93
- [32] Hockey B J 1971 Plastic deformation of aluminum oxide by indentation and abrasion *J. Am. Ceram. Soc.* **54** 223–31
- [33] Tymiak N I and Gerberich W W 2007 Initial stages of contact-induced plasticity in sapphire: I. Surface traces of slip and twinning *Phil. Mag.* **87** 5143–68
- [34] Tymiak N, Chrobak D, Gerberich W, Warren O and Nowak R 2009 Role of competition between slip and twinning in nanoscale deformation of sapphire *Phys. Rev. B* **79** 174116
- [35] Clayton J D, Bammann D J and McDowell D L 2005 A geometric framework for the kinematics of crystals with defects *Phil. Mag.* **85** 3983–4010
- [36] Lebensohn R A and Tomé C N 1993 A study of the stress state associated with twin nucleation and propagation in anisotropic materials *Phil. Mag. A* **67** 187–206
- [37] Meyers M A, Vohringer O and Lubarda V A 2001 The onset of twinning in metals: a constitutive description *Acta Mater.* **49** 4025–39
- [38] Sneddon I N 1951 *Fourier Transforms* (New York: McGraw-Hill)
- [39] Hirst W and Howse M 1969 The indentation of materials by wedges *Proc. R. Soc. Lond. A* **311** 429–44
- [40] Johnson K L 1970 The correlation of indentation experiments *J. Mech. Phys. Solids* **18** 115–26
- [41] Heo T W, Wang Y, Bhattacharya S, Sun X, Hu S and Chen L Q 2011 A phase-field model for deformation twinning *Phil. Mag. Lett.* **91** 110–21
- [42] Levitas V A, Levin V A, Zingerman K M and Freiman E I 2009 Displacive phase transitions at large strains: phase-field theory and simulations *Phys. Rev. Lett.* **103** 025702
- [43] Acharya A 2001 A model of crystal plasticity based on the theory of continuously distributed dislocations *J. Mech. Phys. Solids* **49** 761–84
- [44] Li C, Borja R I and Regueiro R A 2004 Dynamics of porous media at finite strain *Comput. Methods Appl. Mech. Eng.* **193** 3837–70
- [45] Elder K R and Grant M 2004 Modeling elastic and plastic deformations in nonequilibrium processing using phase field crystals *Phys. Rev. E* **70** 051605
- [46] Zhang W, Jin Y M and Khachaturyan A G 2007 Phase field microelasticity modeling of heterogeneous nucleation and growth in martensitic alloys *Acta Mater.* **55** 565–74
- [47] Zhang W, Jin Y M and Khachaturyan A G 2007 Modelling of dislocation-induced martensitic transformation in anisotropic crystals *Phil. Mag.* **87** 1545–63
- [48] Hu S Y, Henager C H and Chen L-Q 2010 Simulations of stress-induced twinning and de-twinning: a phase field model *Acta Mater.* **58** 6554–64
- [49] Kaga H 1968 Third-order elastic constants of calcite *Phys. Rev.* **172** 900–19
- [50] Skinner A J, LaFemina J P and Jansen H J F 1994 Structure and bonding of calcite: a theoretical study *Am. Mineral.* **79** 205–14
- [51] Bueble S and Schmahl W W 1999 Mechanical twinning in calcite considered with the concept of ferroelasticity *Phys. Chem. Min.* **26** 668–72
- [52] Rohl A L, Wright K and Gale J D 2003 Evidence from surface phonons for the (2×1) reconstruction of the $(1\ 0\ 1\ 4)$ surface of calcite from computer simulation *Am. Mineral.* **88** 921–5
- [53] Hill R 1952 The elastic behavior of a crystalline aggregate *Proc. Phys. Soc. Lond. A* **65** 349–54
- [54] Redfern S A T and Angel R J 1999 High-pressure behaviour and equation of state of calcite, CaCO_3 *Contrib. Min. Petrol.* **134** 102–6
- [55] Birch F 1978 Finite strain isotherm and velocities in single-crystal and polycrystalline nacl at high pressures and 300 K *J. Geophys. Res.* **83** 1257–66
- [56] Vo Thanh D and Lacam A 1984 Experimental study of the elasticity of single crystalline calcite under high pressure (the calcite I–calcite II transition at 14.6 kbar) *Phys. Earth Planet. Inter.* **34** 195–203
- [57] Zouboulis E S and Grimsditch M 1991 Refractive index and elastic properties of single-crystal corundum ($\alpha\text{-Al}_2\text{O}_3$) up to 2100 K *J. Appl. Phys.* **70** 772–6

- [58] Winey J M, Gupta Y M and Hare D E 2001 R-axis sound speed and elastic properties of sapphire single crystals *J. Appl. Phys.* **90** 3109–11
- [59] Lagerlof P D, Mitchell T E and Heuer A H 1984 Stacking fault energy in sapphire (α -Al₂O₃) *Acta Metall.* **32** 97–105
- [60] Kenway P R 1993 Calculated stacking-fault energies in α -Al₂O₃ *Phil. Mag. B* **68** 171–83
- [61] D'Amour H, Schiferl D, Denner W, Schulz H and Holzapfel W B 1978 High-pressure single-crystal structure determinations for ruby up to 90 kbar using an automatic diffractometer *J. Appl. Phys.* **49** 4411–6
- [62] Sato Y and Akimoto S 1979 Hydrostatic compression of four corundum-type compounds: α -Al₂O₃, V₂O₃, Cr₂O₃, and α -Fe₂O₃ *J. Appl. Phys.* **50** 5285–91
- [63] Kronberg M L 1968 A structural mechanism for the twinning process on {1012} in hexagonal close packed metals *Acta Metall.* **16** 29–34
- [64] Reinhart W D, Chhabildas L C and Vogler T J 2006 Investigating phase transitions and strength in single-crystal sapphire using shock-resock loading techniques *Int. J. Impact Eng.* **33** 655–69
- [65] Hill R, Lee E H and Tupper S J 1947 The theory of wedge indentation of ductile materials *Proc. R. Soc. A* **188** 273–89
- [66] Zhang R Y, Daymond M R and Holt R A 2008 A finite element model of deformation twinning in zirconium *Mater. Sci. Eng. A* **473** 139–46

NO. OF
COPIES ORGANIZATION

1 (PDF only)	DEFENSE TECHNICAL INFORMATION CTR DTIC OCA 8725 JOHN J KINGMAN RD STE 0944 FORT BELVOIR VA 22060-6218
1	DIRECTOR US ARMY RESEARCH LAB IMNE ALC HRR 2800 POWDER MILL RD ADELPHI MD 20783-1197
1	DIRECTOR US ARMY RESEARCH LAB RDRL CIO LL 2800 POWDER MILL RD ADELPHI MD 20783-1197
1	DIRECTOR US ARMY RESEARCH LAB RDRL CIO MT 2800 POWDER MILL RD ADELPHI MD 20783-1197
1	DIRECTOR US ARMY RESEARCH LAB RDRL D 2800 POWDER MILL RD ADELPHI MD 20783-1197

NO. OF
COPIES ORGANIZATION

ABERDEEN PROVING GROUND

58 DIR USARL
RDRL CIH
R NAMBURU
RDRL CIH C
P CHUNG
J CLARKE
D GROVE
J KNAP (10 CPS)
RDRL WM
B FORCH
S KARNA
J MCCAULEY
P PLOSTINS
RDRL WML B
I BATYREV
B RICE
N WEINGARTEN
RDRL WML H
B SCHUSTER
RDRL WMM B
G GAZONAS
D HOPKINS
B POWERS
RDRL WMM E
C HILTON
J SWAB
RDRL WMM G
J ANDZELM
RDRL WMP
S SCHOENFELD
RDRL WMP B
R BECKER
S BILYK
D CASEM
J CLAYTON (10 CPS)
D DANDEKAR
M GREENFIELD
C HOPPEL
Y HUANG
R KRAFT
R LEAVY
B LOVE
D POWELL
M RAFTENBERG
S SATAPATHY
M SCHEIDLER
T WEERASOORIYA
C WILLIAMS

NO. OF
COPIES ORGANIZATION

RDRL WMP C
T BJERKE
S SEGLETES
RDRL WMP F
N GNIAZDOWSKI

INTENTIONALLY LEFT BLANK.